TIME-RESOLVED IN-SITU ANALYSIS OF

DENSIFICATION OF NANO-BORON CARBIDE

UNDER SUPERIMPOSED ELECTRIC AND THERMAL FIELDS

WITH ENERGY DISPERSIVE X-RAY DIFFRACTION

by

Hulya Bicer

A Dissertation submitted to the

Graduate School-New Brunswick

Rutgers, The State University of New Jersey

in partial fulfillment of the requirements

for the degree of

Doctor of Philosophy

Graduate Program in Materials Science and Engineering

written under the direction of

Professor Thomas Tsakalakos

and approved by

_____

_____

_____

_____

_____

New Brunswick, New Jersey

January, 2016

ABSTRACT OF THE DISSERTATION

TIME-RESOLVED IN-SITU ANALYSIS OF

DENSIFICATION OF BORON CARBIDE

UNDER SUPERIMPOSED ELECTRIC AND THERMAL FIELDS

WITH ENERGY DISPERSIVE X-RAY DIFFRACTION

by Hulya Bicer

Dissertation Director: Professor Thomas Tsakalakos

Boron carbide (B_4C) is characterized by high melting temperature, high hardness, and low density. Such exceptional properties make B_4C is an important covalent solid which is considered the foremost material of choice for high-technology applications. However, low diffusivity caused by the highly directional and stiff character of the covalent bond makes the thermally activated sintering of B_4C difficult. Highly covalent bonded ceramics are sintered with hot pressing and spark plasma sintering (SPS) to achieve high densities. However, these two techniques are limited to simple shape components and costly, involving expensive equipment. Pressureless sintering of B_4C is desired to avoid expensive die designs and post sintering diamond machining, but very high sintering temperatures close to melting point is necessary to obtain high densities.

Recently introduced flash sintering technique is a low voltage two electrode method which enhances the densification of ceramics. The sintering time and temperature can be reduced substantially with flash sintering that provide essential energy savings. In this study, the feasibility of flash sintering of nanoparticulate boron carbide is investigated. Firstly, we analyze the thermal expansion of boron carbide under different constant electric field strength to obtain

fundamental data to provide insight into understanding of flash sintering. The electric field strength has an effect on the non-linear thermal expansion coefficients of B_4C, and expansion becomes more non-linear with the increase of applied e-field. Secondly, the variety of non-isothermal and isothermal flash sintering experiments have been performed to achieve densification of B_4C. By using low voltage, densities up to 95% of the theoretical density have been accomplished at temperatures as low as 711^oC and short times on the order of few minutes. The very low process densification temperatures and time clearly indicate that mass transport in this nanoparticulate system under the action of both thermal and electrical fields are of an electrochemical origin. The implementation of ultrahigh energy EDXRD method in flash sintering of B_4C enables us to monitor the evolution of nanoparticulate matter at the unit cell scale that is otherwise not possible with conventional Bragg-Brentano-method. EDXRD analysis reveals the transient anomalous unit cell expansion which is consistent with the flash sintering phenomena, and we demonstrate that flash sintering of B_4C is possible with help of new coupling mechanism called the galvanomechanical effect. Moreover, we investigate the effect of different flash sintering conditions on densification of B_4C.

Acknowledgment

I would like to thank my advisor Dr. Thomas Tsakalakos for his guidance, constant support and trust he showed me throughout this study. I am also truly grateful to Dr. Koray Akdogan for his endless contribution and help for my research. Furthermore, I wish to express my gratitude to Dr. Zhong Zhong, Dr. Lisa C. Klein, and Dr. Frederic Cosandey for agreeing to participate in this thesis committee. I also thank Dr. Zhong again for his enormous help during our work at Brookhaven National Laboratory.

I sincerely thank past and current Nanomaterials Laboratory group members, Ilyas, Tevfik, Bart, undergraduate students, William, and Ms. Kathleen for their help in my experiments and fun environment they provided in laboratories at Rutgers, BNL, and ANL.

I am thankful to many people at MSE department for their help and support during my studies. I thank to Dr. Dunbar Birnie, Dr. Lisa Klein, Dr. John Mathewson, and MSE staff for making my adjustment to academic life at Rutgers much easier. Many thanks to my colleagues for their support and close friendship: Berra, Rut, Elaheh, Fatih, Metin, Muharrem, Azmi, Zeynep, Ibrahim, Vishnu.

I have gained lots of wonderful friends during my stay in US and they have been my family since then. We have shared our sadness and joy miles away from home that I will never forget.

Lastly, but most importantly, I owe so much to my family who supported my decision to travel oversea to pursue my academic career. The loss of my father during my study affected us deeply, but the love, support and prayers from my family and friends helped and encouraged me to return my work and complete my dissertation effectively.

Also, I would like to acknowledge the funding sources that allowed me to study without financial concerns. I would like to thank Turkish Ministry of National Education Fellowship, the Office of Naval Research under contract no. N00014101042 and N000141512492, and Department of Energy Office under contract no. DEAC0206CH11357. Significant contributions were made by Dr. A. Makinen and Dr. L. Kabacoff of the ONR and Dr. J. Okasinski of ANL with respect to valuable technical feedbacks.

Table of Contents

List of Tables

List of Figures

1. Introduction

Boron carbide is an important non-oxide material with high melting temperature, outstanding hardness, high neutron absorption cross-section, and light weight. Such unique combination of properties make B_4C good candidate in structural ceramic applications (armor material, wear-resistant components, and reactor control rods). However, due to the highly covalent nature of B_4C, it has very low sinterability. Conventional densification of B_4C has been performed mostly with hot pressing of high quality powder with temperatures ≥ 2200^oC and 12-48 hours. Therefore, densification of B_4C without pressure requires even higher temperatures and very long sintering time [2-11].

The electric field assisted sintering has effect on thermodynamics and kinetics of densification mechanisms. Spark plasma sintering (SPS) is one of the field assisted sintering techniques that reduce sintering temperature and time compared to other conventional methods. The application of additional thermodynamic driving force, which is the application of high power in SPS, provides additional energy to particulate matter. SPS is steady state process which is based on Joule heating. The disadvantage of SPS is that the equipment used in technique is expensive and it is limited to simple shape components [67-70].

The recently discovered flash sintering which is based on two electrode method shows profound development in sintering technologies. It has been shown in several studies that the radical reduction in sintering temperatures with the application of very low fields can be accomplished on time scales that are at least 1-2 orders of magnitude

shorter than conventional methods. Most of the flash sintering studies up to date have been performed with oxide ceramics and there is not enough study on the flash sintering of covalent bonded materials, except preliminary results on SiC and ZrB_2. In this study, the densification of highly covalent boron carbide with two electrode flash sintering method is attacked to reduce sintering temperature and time in an absence of pressure [90-95].

The unique experimental method used in this study is energy dispersive x-ray diffractometry (EDXRD) with an ultrahigh energy polychromatic synchrotron probe which has strong penetration; therefore, the diffraction data can be collected from body center of the sample of interest. A time resolved in-situ EDXRD study of flash sintering of boron carbide is reported herein, enabling one to observe the evolution of densification at the unit cell level in addition to well established macroscopic description.

2. Literature Review

2.1. Boron Carbide

Boron carbide is a polaron conductive covalent bonded ceramic which exhibits very attractive properties for high-technology applications. Properties and applications of B_4C will be reviewed in this chapter.

2.1.1. Phase Diagram and Crystal Structure of B_4C

A commonly accepted phase diagram of boron and carbide, which was developed by Beauvy, is depicting boron carbide (B_4C) as the stoichiometrically stable phase between 8.8 at % to 20 at % (see figure 2.1). The melting temperature of B_4C is reported as 2450^oC. In the carbon rich region (C % ≥ 21.6), there is a eutectic point at 29 at.%C,

2375°C. In the boron rich region, there is a peritectic point of 0.1-0.2 at.%C at 2075°C [1-6].

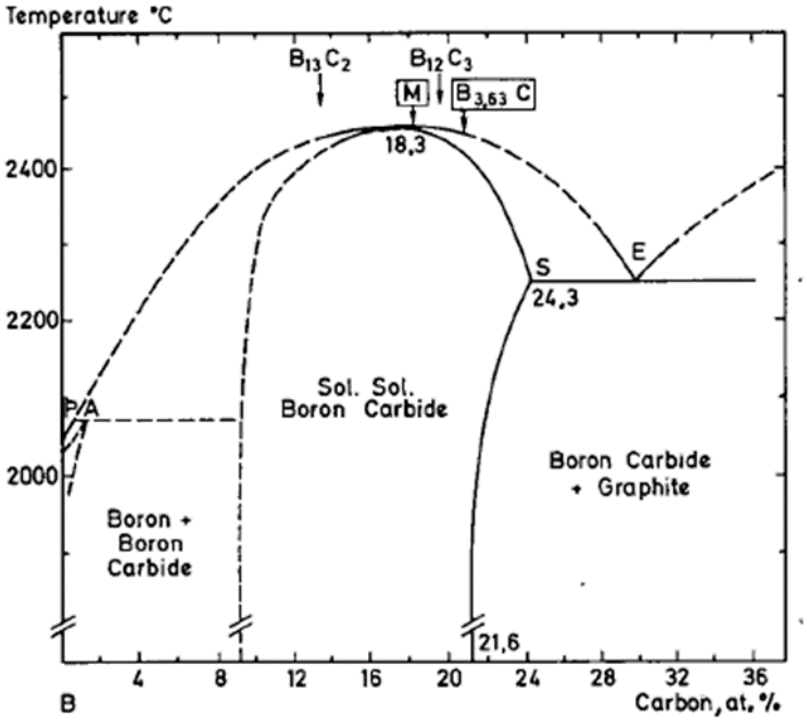

Figure 2. 1. Phase diagram of the boron-carbon system as proposed by Beauvy [1].

In the compositional range of $0.088 \leq x \leq 0.200$ boron carbide crystallizes ($B_{1-x}C_x$) with rhombohedral structure D^5_{3d} – $R\bar{3}m$. The structure consists of 15 atoms; 12-atoms on the corners of the deformed icosahedra and linear 3-atom chains, and the atoms on icosahedra are connected with covalent bond to atoms in neighboring icosahedra (Fig. 2.2). Occupancies of sites in the structure by carbon and boron atoms are controversial because of electronic scattering cross-section similarities of boron and carbon isotopes. Therefore, most characterization techniques are inadequate to fulfill this identification. There are four different atomic configurations that are proposed in the literature; the

chain model (CCC chain, B12 icosahedron), the polar model (CBC chain, B11C icosahedron), the equatorial model (CBC chain B11C icosahedron model), the same configuration with the equatorial model but C in polar site (CCB chain, B11C icosahedron). The accepted stable phase of B_4C stoichiometry with 20 mole % carbon is mostly identified with B12 (CCC) configuration [7].

The lattice parameters of the rhombohedral boron carbide unit cell can be computed from parameters of the hexagonal unit cell which is considered to be easier than solving complicated rhombohedral system. As shown in Figure 2.3, a_1 (H), a_2 (H), and c (H) axes of the hexagonal cell can be assigned as rhombohedral axes of a_1 (R), a_2 (R), a_3 (R). Boron carbide has hexagonal lattice parameters a_0=5.60 Å and c_0= 12.07 Å with c_0/a_0= 2.155 Å. Size of the boron and carbon atoms are close enough that they can substitute each other. However, as boron is replaced by carbon, the unit cell of boron carbide shrinks slightly due to the small difference between atomic radius of boron and carbon [8, 9].

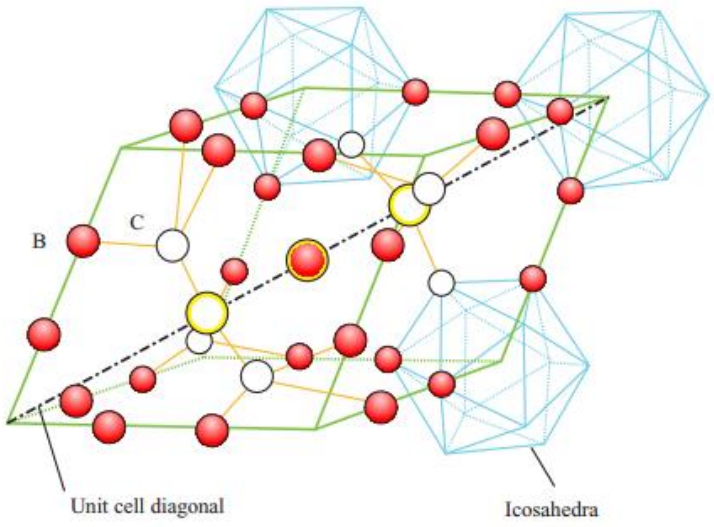

Figure 2. 2. The crystal structure of boron carbide, showing boron and carbon atoms that are distributed within icosahedra [7].

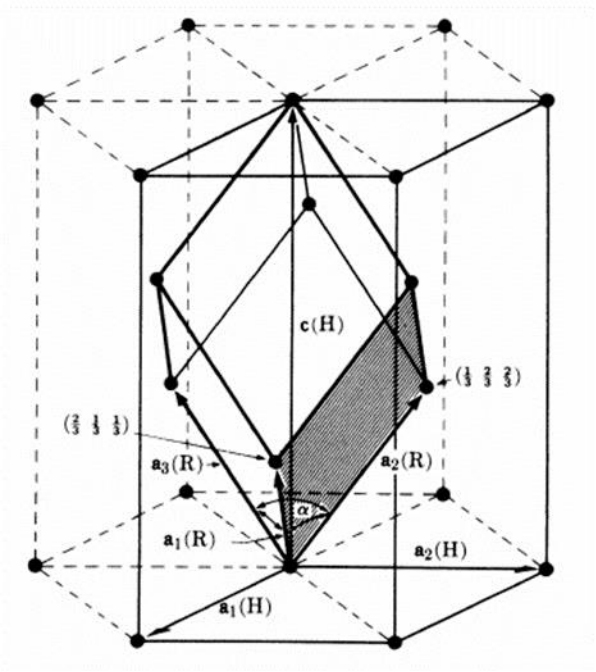

Figure 2. 3. Schematic showing the interrelation between rhombohedral and hexagonal unit cells [8].

2.1.2. Chemical Properties of B_4C

Boron carbide is chemically inert to most organic compounds, and it has very good resistance to acids and alkalis. The weight loss arises from exposition of B_4C to widely used mineral acids and bases is very limited in B_4C system. Hydrofluoric-sulfuric (/nitric) acids mixture attacks B_4C slowly. B_4C also reacts with O_2 at elevated temperatures (around 600^{o}C), and such reaction grows into serious point at 800^{o}C and 1000^{o}C. Oxidation starts with formation of glassy B_2O film on the surface of the particles. Hot oxidizing acids and fused salts lead oxidation of boron carbide. Chlorine and bromine attacks occur at 600^{o}C and 800^{o}C, respectively [10-11].

2.1.3. Physical Properties of B_4C

2.1.3.1. X-ray Density

One of the most important properties of boron carbide is its low density as compared to other structural materials such as alumina, silicon carbide, etc.. With increasing carbon content, the density of B_4C increases linearly in the compositional range of 8.8 at.% - 20.0 at. %. Boron carbide with 20 at. % C has a density of 2.52 gr/cm^3. A widely accepted equation showing the relationship between carbon content and density is [10];

$$d\ (\frac{g}{cm^3}) = 2.422 + 0.0048\ [C]\ at.\% \tag{2.1}$$

The low density of B_4C makes it an important structural material for defense applications as it concomitantly exhibits ultrahigh hardness, high conductivity (electrical and thermal), and high melting temperature [4, 10].

2.1.3.2. Thermal Expansion Coefficient of B_4C

The lattice parameters of rhombohedral (or hexagonal) B_4C increases nonlinearly with temperature, which can be modeled by the use of a second order polynomial of temperature. The average thermal expansion coefficient in the temperature range of 298-1073 K is reported as 4-8 10^{-6} in Thevenot's review paper, while Pilladi has reported average thermal expansion coefficients in the temperature range of 298-1773 K for nano and microcrystalline boron carbides as 7.76×10^{-6} K^{-1} and 7.06×10^{-6} K^{-1}, respectively [10,14,15].

2.1.3.3. Thermodynamic Properties of B_4C

Table 2.1 shows the calculated thermodynamic properties of boron carbide, such as heat capacity, entropy, free energy function, and enthalpy change. Matsui reported that the heat capacity and electrical conductivity of B_4C were measured by direct heating pulse calorimetry and thermal conductivity of B_4C was calculated from the heat capacity values and thermal diffusivity data from [17]. Such information for B_4C was for analyzing the energetics of the burst mode sintering in B_4C as discussed in section 6. The temperature dependence of isobaric heat capacity is reported as (T in Kelvin);

$$c_p(cal/molK) = 22.99 + 5.40x10^{-3}T - 10.72x10^{5}T^{-2}$$ [10].

Table 2. 1. Thermodynamic quantities of B_4C [16].

T (K)	C_p ($J\,mol^{-1}K^{-1}$)	S^0 ($J\,mol^{-1}K^{-1}$)	$-(G_T^0 - H_{298}^0)/T$ ($J\,mol^{-1}K^{-1}$)	$H_T^0 - H_{298}^0$ ($J\,mol^{-1}$)
298.15	49.82	27.18	27.18	0
300	50.30	27.49	27.18	93
400	72.52	45.20	29.45	6302
500	86.88	63.05	34.39	14327
600	96.20	79.77	40.58	23512
700	102.74	95.11	47.29	33476
800	107.73	109.17	54.16	44009
900	111.82	122.10	61.00	54992
1000	115.38	134.07	67.72	66355
1100	118.62	145.22	74.26	78057
1200	121.68	155.68	80.61	90074
1300	124.61	165.53	86.77	102388
1400	127.47	174.87	92.73	114993
1500	130.29	183.76	98.51	127881
1600	133.09	192.26	104.10	141051
1700	135.88	200.41	109.53	154499

2.1.3.4. Thermal Conductivity of B_4C

Boron carbide is a good thermoelectric material for high temperature applications because of its high thermal conductivity. Figure 2.4 depicts the thermal conductivity of boron carbide as a function of temperature and carbon concentration. Boron carbides

with lower carbon concentration have smaller thermal conductivities and show weaker temperature dependence. That is because unoccupied sites by carbon distort the B_4C lattice. On the other hand, boron carbides with higher carbon concentration (x=0.2, B_4C) exhibit high thermal conductivity (298K, 30W/m.K) since carbon atoms occupy all sites, resulting a well ordered structure. In such boron carbides, the thermal conductivity of B_4C decreases with increasing temperature [17-20].

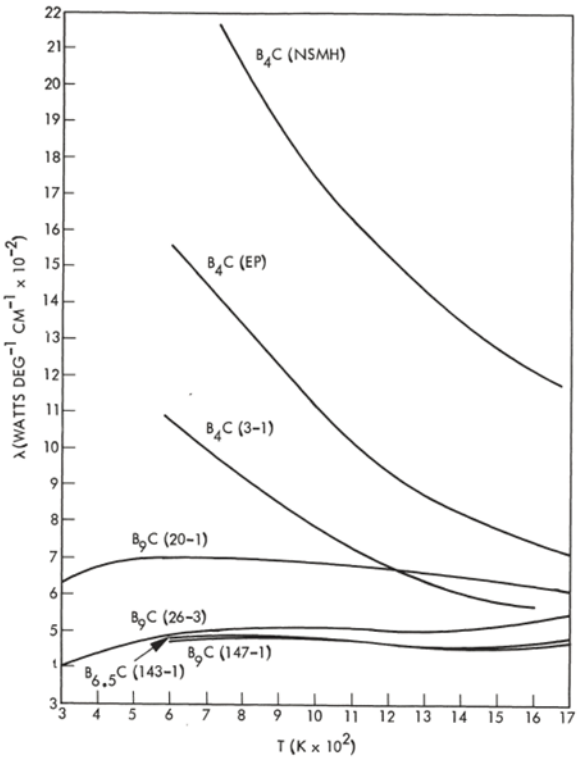

Figure 2. 4. The thermal conductivity of boron carbide as a function of temperature and carbon concentration [17].

2.1.3.5. Electrical Properties of B_4C

The energy band scheme of boron carbide is depicted in fig. 2.5. There are various reported in the literature for the band gap of B_4C; Werheit reported Eg=2.09 eV as seen

in the fig. 2.5 based on optical absorption, luminescence, and transport properties. The reported exciton energy is 1.560 eV. Yamazaki reported Eg=2.5 eV originated from occupied and unoccupied sites. The relatively small band gap as compared to other ceramic materials is believed to be the reason for low electrical resistivity of boron carbide [21-23].

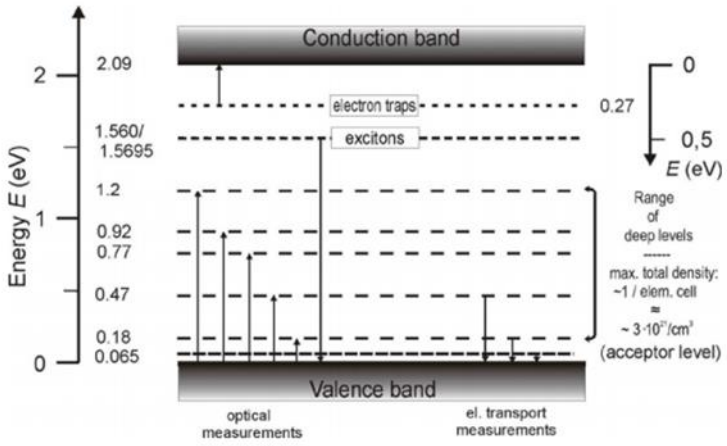

Figure 2. 5. Energy band scheme of Boron Carbide. Arrows indicate the direction of the measured transitions [21, 22].

Reported seebeck coefficients of boron carbide indicate p type conductivity and increase with increasing temperature. Analysis of conductivity with Hall mobility and Seebeck coefficient measurements suggest that the charge carriers are holes in boron carbide, and such carriers form small polarons. Polarons move through the crystal structure by phonon assisted hopping motion between inequivalenty located carbon atoms. The effect of the pressure on this motion is significant due to decrease of intericosahedral distance with application of pressure. Hence the increase of hopping activation energy with increasing pressure. Figure 2.6 shows the temperature dependence of the electronic conductivity of B_4C at different pressures. The graph also

depicts the conductivity behavior as a function of temperature [24]. The conductivity of B_4C increases with an increase in temperature. The temperature dependence of electrical conductivity by the small polaron hopping mechanism of B4C conventionally expressed as;

$$\alpha = \frac{A}{T} exp\left(-E_a / kT\right) \tag{2.2}$$

where A is the pre-exponential factor, k is Boltzmann constant, and E_a is the activation energy.

As the temperature increases above 400 K, the temperature dependence of the conductivity changes slightly from non-Arrhenius to Arrhenius behavior. Activation energy of the boron carbide conductivity is 0.16 eV in the Arrhenius regime. At very high temperatures (1400 K - 1750K) the conductivity increases sharply and follows a power law. The temperature dependence of the hopping conductivity decrease and due to high temperature and high carrier density saturation of hopping conductivities and hopping suppression are observed. In this regime, activation energy increases to 0.6 eV. Such electrical conductivity behavior can be explained by the small polaron hopping conductivity [25, 26].

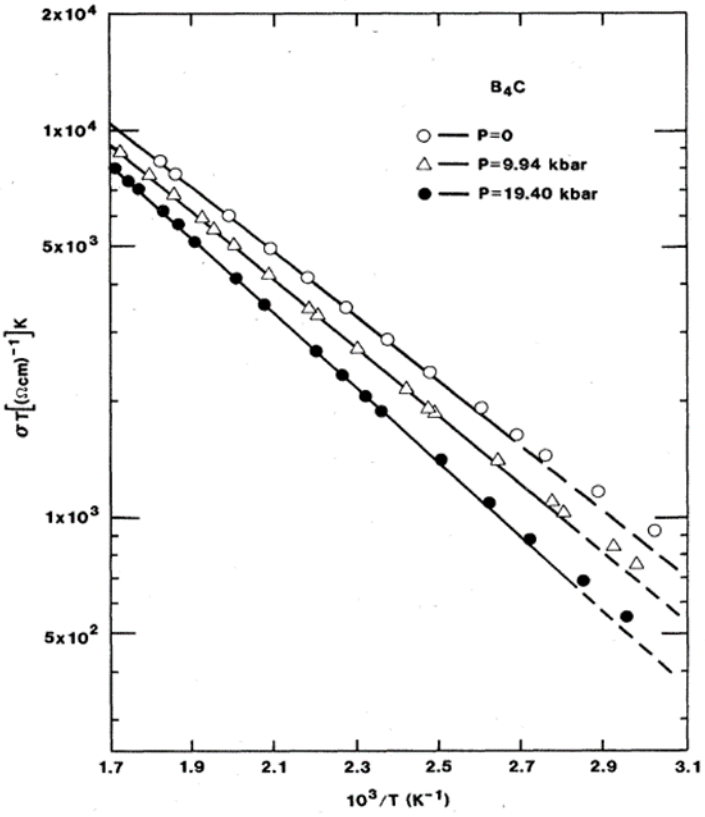

Figure 2. 6. Arrhenius plot showing the temperature dependence of the electronic conductivity of B4C at three pressure [24].

2.1.3.6. Mechanical Properties of B_4C

Boron carbide is among the hardest materials; third one after diamond and cubic boron nitride. Besides its outstanding hardness it has low density which makes it very desirable for applications requiring low inertia such as ballistic armor. The preparation method, stoichiometry, porosity, and impurity content affect the mechanical properties of boron carbide as any other ceramic materials. Table 2.2 compares mechanical properties of hot pressed and pressureless sintered B_4C so as to emphasize the importance of processing at mechanical properties.

Table 2. 2. Properties of hot pressed and pressureless sintered samples [33].

Property	*Hot-pressed B_4C*	*Sintered B_4C*	
		B_4C–1wt.%C	*B_4C–3wt.%C*
Total carbon content[a] (wt.%)	21.7	22.5	24.8
Porosity (%)	<0.5	<2	<2
Bulk density (g cm^{-3})	2.51	2.44	2.46
Mean grain size (μm)	5	8	7
Flexural strength (four-point bend) (MN m^{-2})	480 ± 40	351 ± 40	353 ± 30
Young's modulus (GPa)	441	390	372
Shear modulus (GPa)	188	166	158
Poisson's ratio	0.17	0.17	0.17
Fracture toughness (K_{Ic} (SENB)) (MPa $m^{1/2}$)	3.6 ± 0.3	3.3 ± 0.2	3.2 ± 0.2

Deviation from the B_4C (B12 icosahedra, C3 chain) alters mechanical properties in the B-C system. As in content increase in boron in the B_4C structure reduces hardness and fracture toughness by diminishing bond strength between B and C groups. B_4C with %20 C provides the highest hardness and fracture toughness. Nevertheless, fracture toughness of B_4C is low and is only 3-4 $MPam^{1/2}$. The Knoop micro-hardness is HK_{200g} =29±1.5 GPa in hot-pressed samples of B_4C. The elastic modulus and shear modulus also vary with boron carbide stoichiometry and decrease with increasing B in the boron carbide structure. The elastic modulus, shear modulus, and poison ratio of B_4C (20% C) are typically reported as 450-470 GPa, 188-200 GPa, and 0.14-0.18, respectively.

Porosity and grain size also affect the mechanical properties of boron carbide. Increase in the porosity and grain size decrease the strength profoundly. Porosity leads to the failure at low stress levels, which is why sintering of boron carbide to higher densities is extremely important [27-35].

2.1.4. Applications of B_4C

During the Vietnam War, ceramic armor utilizing Al_2O_3, SiC, AlN, B_4C, and TiB_2 was developed by the DOD for the US Military to protect helicopter pilots and key payload. Today, B_4C is considered the best ceramic armor due to its outstanding hardness and low density. Table 2.3 provides a comparison between properties of most common ceramics for armor applications. In 1966, first boron carbide personnel armor was developed for the ground operations. For instance a quarter inch plate of B_4C can stop a 30 caliber armor piercing projectile with a tungsten carbide core [36-39].

Table 2. 3. Critical properties of common armor ceramics (37).

Property	unit	SiC	B_4C	Al_2O_3
Density	g/cc	3.13	2.45	3.45-3.9
Hardness	Knoop	2800	2850	2260
Young's Modulus	$x10^6$ psi	59	65	54
Sonic Velocity	meter/sec	11500	13000	5000
Flex Strength	$x10^3$ psi	67	50	40

Boron carbide is also used for borinizing of steel so as to harden steel surface. In this process boriding mixture, which consists of the boriding agent (B_4C), the activator (fluoroborate), the diluent (SiC), and metal are heated to ~900-1000^oC [40, 41]. Moreover, B_4C is used in sand blasting technology- a surface treatment process which is used for surface modification and surface strengthening-. Maximum efficiency can be achieved with B_4C abrasive air jet nozzle because of low wear rates and long lifetime of B_4C nozzle. Hence, optimization of cost and performance makes B_4C most favorable material for sand blasting process [42-44].

In the nuclear industry, boron carbide has been used as control rod, shielding material, and as neutron detector because of its high thermal neutron capture cross section of the ^{10}B isotope. Boron carbide is resistant to radiation damage, and exhibits self-healing properties against secondary damage caused by radiation. Its high melting point provides integrity within the core of the nuclear reactor [45-47].

2.2. Sintering and Densification of B_4C

Sintering is the process in the fabrication of technical and conventional ceramics in which the shaped powder is heated to a temperature around ¾ of the absolute melting point to induce densification so as to obtain a desired end density. In other words sintering causes a particulate compact to transform into a dense polycrystalline solid with some residual porosity.

2.2.1. A Brief Review of Sintering Theory, Stages and Mechanisms

Sintering is thermally activated and time dependent process under the driving force of which is the excess surface energy of a particulate system. The driving force is due to i) surface curvature, ii) outward pressure, and iii) gradients in chemical composition. In particulate system, individual small particles with large surface area promote the forming joining point which are called necks that eventually lead to the formation of grain boundaries. The neck formation causes stress gradients across the particles, which influences the local chemical potential of the atoms, causing mass transport towards neck to eliminate stress (also known as sintering stress). [39, 48-50].

Sintering is accompanied by continues change in microstructure until densification stops. Traditionally, sintering thought to take place in three stages; the initial,

intermediate, and final stage. In the initial stage, there is an increase in the interparticle contact area due to neck formation at the contact points. In this stage, specimen densifies by ~10%. In the intermediate stage, particle contact area grows and pores become interconnected along the grain edges. Most of the increase in density occurs in this stage, which is corresponds to additional densification by ~30%, or to a total of about 95% of the theoretical density (TD). Small isolated pores on the grain boundaries and in the grains may remain at the end of this stage. Final stage begins around 95% of the TD when pores are isolated at the grain corners. Elimination of the porosity along grain edges is done with mass transport through grain boundaries, but this could also give rise to grain growth since this process requires broad time. Pore elimination in the final stage increases the density to ≥ 99% of the TD at the end of this stage [48, 51-55].

Mass transport can occur via different paths but not all paths result in densification. Each path corresponds to a different mass transport, and these paths are called the sintering mechanisms. Some of these mechanisms lead to densification while the non-densifying mechanism have indirect effect on the densification rate by promoting mass transport (diffusion) mechanisms. Such diffusion routes are depicted in Fig. 2.7.

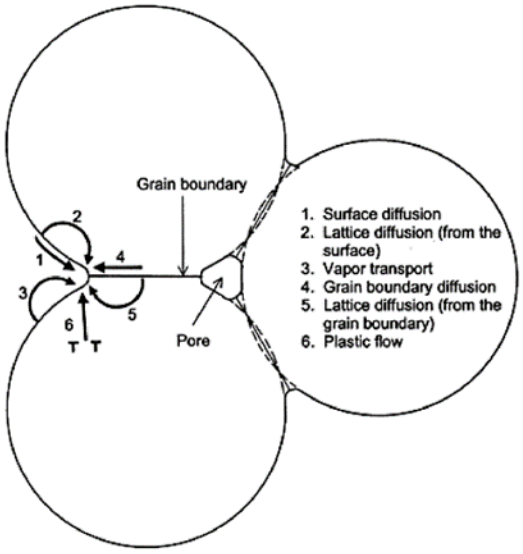

Figure 2. 7. The mass transport paths and the associated six mechanisms – surface diffusion, lattice diffusion (from the surface), vapor diffusion, grain boundary diffusion, lattice diffusion (from the G.B.), and plastic flow- [48].

Surface diffusion, lattice diffusion from surface, and vapor transport (evaporation and condensation occur at surface of the particles) mechanisms involve neck growth without causing densification. However, they are still important since they reduce the curvature of neck surface (driving force for sintering). At the beginning of densification, surface diffusion is controlling the process since surface atoms have weaker bonds. Hence, the activation energy for surface diffusion is lower than other sintering mechanisms. Grain boundary diffusion and lattice diffusion from grain boundary are essential for densification to become a dense polycrystalline materials. These paths lead to shrinkage and densification. Mass transport is originating in the particle volume or at the grain boundary, and the matter is moving from grain boundaries to pores which are on or near grain boundary. If plastic flow is possible as in the ease of alloys, mass transport

along dislocations (dislocation type diffusion) within the neck region takes place, which is also considered as a densifying mechanism [56,57].

The increase in the average grain size is in polycrystalline materials called as grain growth. In the content of sintering, grain growth is closely related to analyze pore-grain boundary interaction. Mass transport occurs from grain boundaries to the pores, and pore shrinkage is accompanied by grain growth. Higher densification can be achieved with restraint of grain growth. That is so because grain growth also consumes the excess surface free energy but does not result in densification (see Fig. 2.8).

The commonly accepted phenomenological equation describing grain growth is;

$$\frac{1}{\rho}\frac{d\rho}{dt} = \frac{K}{G^m} \tag{2.3}$$

where G is grain size, ρ is density, m is equal to 3 for lattice diffusion and 4 for grain boundary diffusion, and K=$(2\alpha M_b \gamma_{gb})^{1/2}$ with M_b as the mobility of the grain boundary, γ_{gb} as the specific grain boundary energy, and α as a geometrical constant which depends on shape of the boundary. The radius of grain boundary curvature is inversely proportional to grain growth, the resulting in a typical grain growth law in the form;

$$G - G_0 = K\, t^n \tag{2.4}$$

where n varies from 1/3 to 1/2, G_0 is the grain size at $t = 0$. As an example, the plot of log grain diameter versus log time for grain growth in high-purity alpha brass is shown in Fig. 2.9. The grain growth follows equation (2.4) until the grain size approaches the limiting which is about 2 mm.

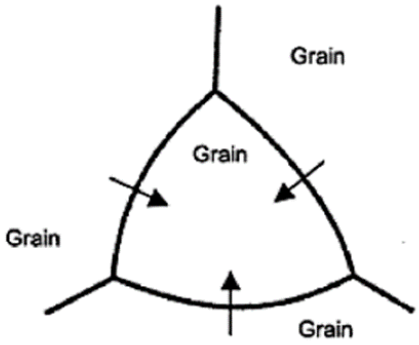

Figure 2. 8. Movement of the grain boundary towards its center of curvature whereby pore volume is minimized and sometimes completely eliminated [48].

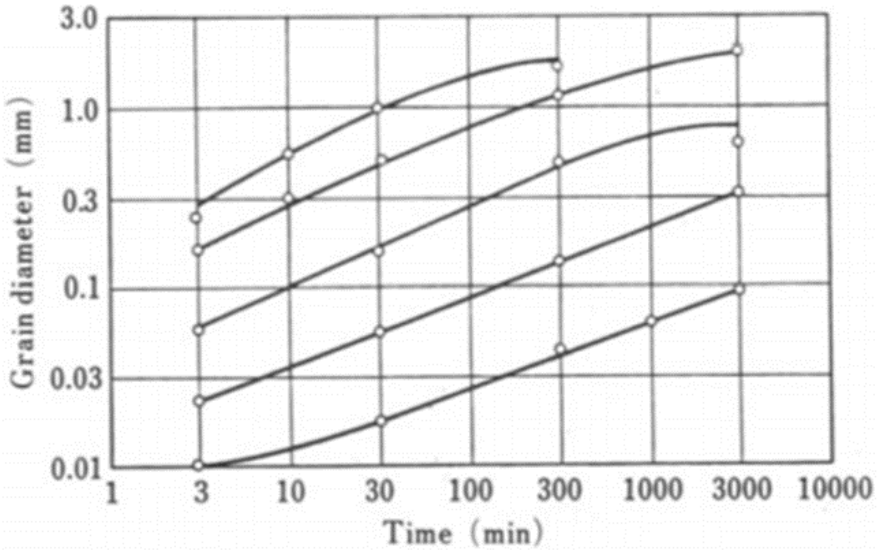

Figure 2. 9. Grain diameter versus time for grain growth in high-purity alpha brass [50].

When grain growth and pore growth occur simultaneously during sintering, it is called as coarsening. Some of the diffusion mechanisms (surface diffusion, vapor transport) mentioned earlier do not lead to densification and instead they cause coarsening of the grain size, reducing the driving force for sintering thereby. Figure 2.10 shows the difference between two microstructure where the dominant mechanism was

densification (a) and coarsening (b), respectively. Figure 2.10.a shows fully dense sample (TD=100%) where all pores are eliminated while Fig. 2.10.b demonstrates a network of pores in the microstructure due to coarsening [58, 59].

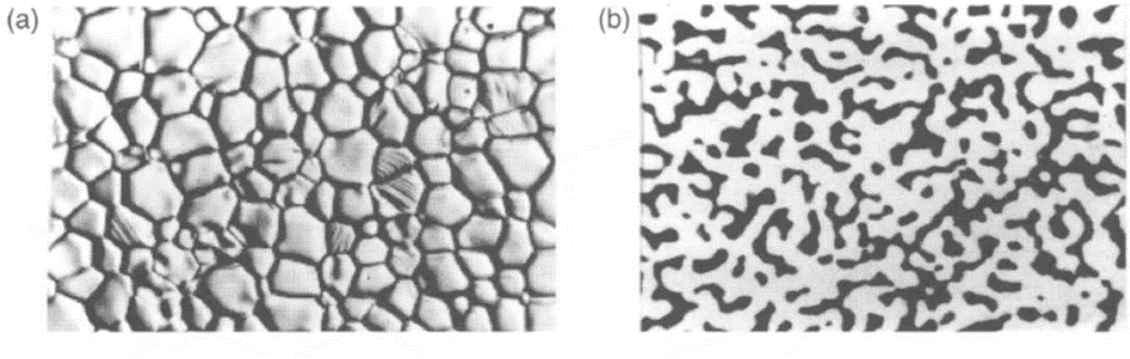

Figure 2. 10. (a) The surface of an Al2O3 ceramic without porosity (b) The sintering of Silicon with a continuous network of solid material (white) and porosity (black) [59].

2.2.2. Sintering of Boron Carbide

Boron carbide is a highly covalent ceramic where atomic mobility is low due to the highly localized bonding and stiff character of the covalent bond. To enhance diffusivity a multitude of processes are used for sintering to promote densification which we as surveyed below.

2.2.2.1. Hot Pressing

Hot pressing is a commercial method for densification of boron carbide. In this process, the die assembly is in high temperature furnace, and the specimen is uniaxially pressed with a static load while heated to a high temperature than isothermally held for a long time. Figure 2.11 shows the basic configuration of hot pressing system. Hot pressing lowers the sintering temperature, and consequently suppresses grain growth or secondary recrystallization, relatively. While hot pressing results in ~100% density and

small grain size (~1micron), hot pressing is very long process, and it is not cost efficient. The dies used in hot pressing are expensive and do not have a long service life. Moreover, hot pressing is limited to forming simple shaped components; such as cylinders and blocks. More complex shaped components require high costs specialty dies. Graphite is the most common die material for hot pressing [60, 61].

B_4C powders are densified >90% theoretical densities under inert atmosphere or vacuum at 2173 to 2473^oK with application of 30-50 MPa for up to 48 hours. Studies show that full densification requires high temperatures >2400K provided that the powder is of good quality. Although high pressure accelerates densification, at very high temperatures it is not as effective and cannot prevent grain growth to any substantial extent.

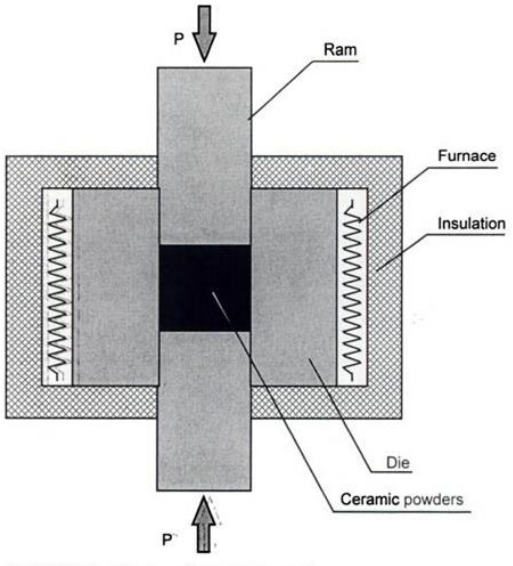

Figure 2. 11. Schematic of hot pressing furnace [61].

An alternative method for sintering B_4C is hot isostatic pressing (HIP) which has advantages over hot-pressing process such as the ability to sinter complex shapes under 3D hydrostatic state of stress. The densification temperature in HIP is relatively lower than

hot-pressing, while the applied pressure usually is 100-300 MPa which is higher than pressures used in hot-pressing. Needless to say, the densification rate is proportional to the magnitude of the applied stress. The needed-hydrostatic pressure is applied in an autoclave using an inert gas. B_4C densification to > 95% at 1200-1750^oC with sintering aids is possible by hot isostatic pressing with 30-60 min [62-67].

2.2.2.2. Current Activated and Pressure Assisted Densification

Here, electric current is used to enhance mass transport and to lower the densification temperature. The electric current may be applied in pulse mode or continuously. A typical apparatus is schematically shown in Figure 2.12. One of the most commonly used electric field assisted sintering technique is spark plasma sintering (SPS). The major differences between SPS and hot pressing are heating rate and heat transfer. In addition to the applied field three main parameters define the SPS process; (i) heating rate, (ii) applied pressure, and (iii) applied current. The uniaxial load as well as the current are applied by pistons made out of graphic. A low voltage (10-15 V maximum), very high current (1000 A to 10,000A) are used, which leads to joule heating which provides the necessary thermal activation for densification. The applied pressure typically varies between 30-200 MPa. The application of electric current enhances the known sintering mechanisms and/or activate new mechanisms via electromigration, increase in point defects concentration, superplasticity, and the reduction of activation for migration of defects. Electric current creates a spark discharge at particle contact points, resulting extreme local heating at particle surfaces. With the SPS technique, even non-conductive materials can be sintered because heat can be transferred to material easily. Grain growth

can be controlled by minimizing the sintering time at high temperature from the graphite die [68-71].

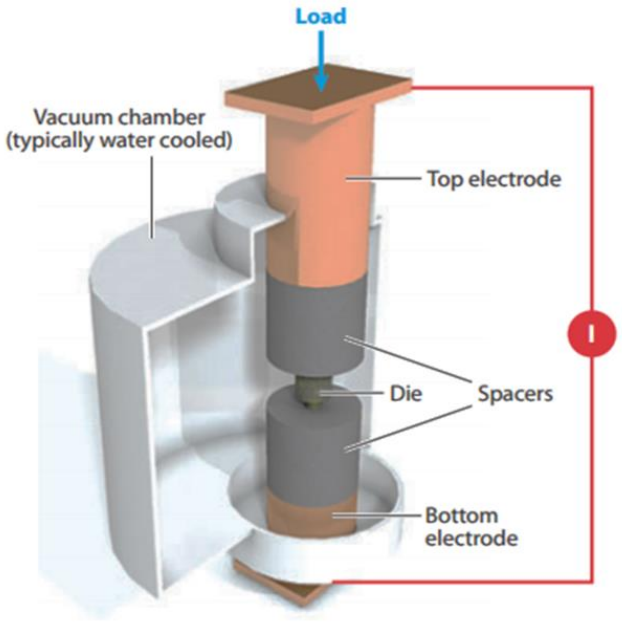

Figure 2. 12. Main components of current activated, pressure assisted densification apparatus [69].

Table 2.4 summarizes the different reported process parameter in SPS for sintering of B_4C. For full densification a temperature over 1800^oC is needed under 30-100 MPa pressure. As expected, the increase in temperature, applied pressure and holding time result in higher density. Hayun, et al (2010) observed grain coarsening at temperatures ~2200^oC. SPS process is also limited to simple symmetrical shaped samples and very high dc current supply is needed which makes SPS a costly hot consolidation process [72-76].

Table 2. 4. SPS parameters for B_4C densification reported in different research articles

Reference	Heating Rate (°C/min)	Temperature (°C)	Hold time (min)	Pressure (MPa)	TD %
Tamburini [72]	200	1600-1700	10	70	98
Sairam [137]	100	1800	5		91
			10		96
			15		full
		1700	15		94.4
Xu [73]	100	1800	5	50	96.9-98.4
Hayun [74]		1900-2200		32	80-full
Hayun [75]	50	2050	10	32	full

2.2.2.3. Pressureless Sintering of B_4C

Densification of boron carbide with traditional sintering methods is extremely difficult due to low diffusivities in covalent solids. Due to the limitation of pressure assisted method in producing complex shape components, pressureless sintering is desirable considered to avoid expensive die designs and post sintering diamond machining. On the other hand, very high temperatures approaching the melting point and very fine powder are required to obtain high densities, but in most cases coarsening is inevitable. Various additives have been used to enhance sintering behavior of B_4C by eliminating pore growth, but the resultant second phases have deleterious effects on mechanical properties. Most commonly used additive is carbon, although dopants such as Al, $AlFe_3$, Ni, Fe, Cu have been used to enhance the sinterability of boron carbide. Coarsening in pressureless sintering of B_4C has been suggested to B_2O_3 layer in starting powders surface. It is believed that the B_2O_3 nondensifying mechanisms in sintering which

leads to coarsening. Addition of carbon eliminates B_2O_3 coating by reducing it carbothermically [77-84].

2.3. Flash Sintering

As explained in the previous section, it is extremely difficult to densify B_4C without pressure assistance. Early work on 3 % ytrria doped zirconia by Raj and Conrad shows drastic reduction in sintering temperature with a low dc electric field (20V/cm), also keeping the grain size small due to faster sintering rates[85]. The recently discovered flash sintering method by Cologna and Raj has shown that with application of sufficient electric field directly to a sample can reduce sintering temperature several hundred degrees below conventional sintering and reduce sintering time from hours to seconds. Flash sintering requires low power, and it promises exciting reduction in energy consumption for sintering. The method basically consist of applying a DC field across the ceramic body by two electrodes while heating in a furnace [87]. This technique has been demonstrated for wide range of materials including ionic conductors, semi-conductors, and electronic conductors; such as 3Y-TZP and 8Y-TZP [87, 88], Gadolinia-doped Ceria [89], MgO-doped Alumina [90], Co_2MnO_4 [91], $SrTiO_3$ [92], $BaTiO_3$ [93], SnO_2 mixed to MnO_2 [94], SiC [95], etc. Figure 2.13 shows the sintering temperature versus different dc field values, and corresponding shrinkage. In 3Y-TZP two regimes are demonstrated in the graph; first one is at low fields where densification is gradually completed, and in the second regime, increase of dc field lowers sintering temperature, and this second region is called as flash sintering regime. A summary of the behavior exhibited by of 3% Yttria doped zirconia as a function of dc electric field is shown in figure 2.14 where flash sintering was

accomplished at 1275^{o}C and under 75 V/cm [96]. The sudden increase in power which is shown in figure 2.14 (c) is the signature of flash sintering experiment. Here conductivity of the material increases during heating. When peak power is reached the current is limited, and at certain temperature the material absorbs electrical power, and one switches from voltage to current control. Under current control, the system goes into steady state. Flash sintering is divided into three stages by many; (i) the first stage is called as the incubation time which is the region just before the flash, (ii) the second stage is where transient effect occurs and ultimately the system is switched from voltage to current control, and (iii) the last stage is the steady state under current control where joule heating occurs. All stages are represented in figure 2.14. Controllable variables in the flash sintering process are heating rate, electric field, current limitation in power supply, and holding time in the steady state region during overall process [97, 98].

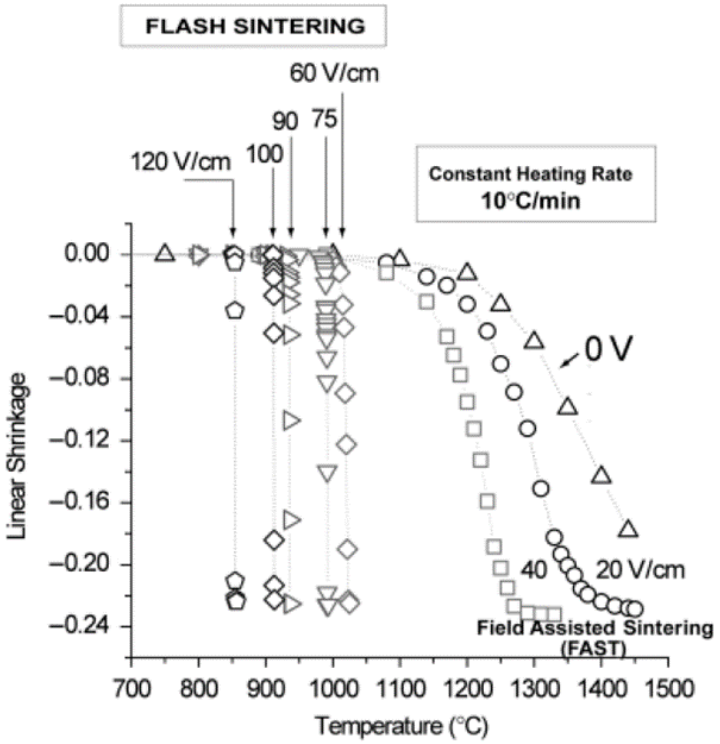

Figure 2. 13. Relation between applied dc fields and sintering temperature [87].

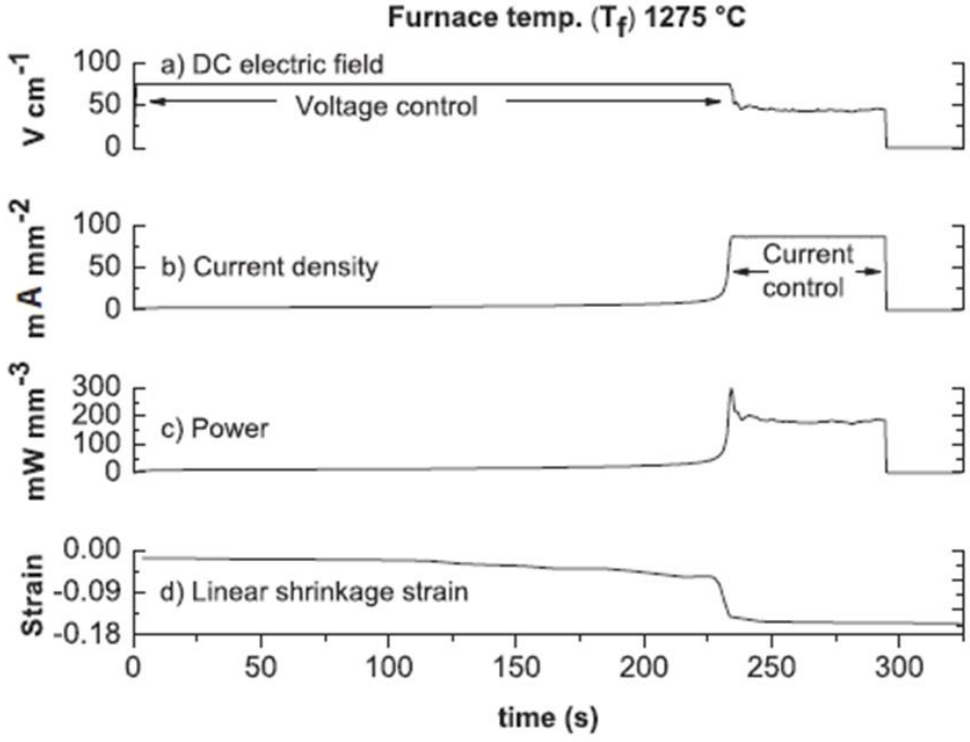

Figure 2. 14. Isothermal flash sintering variables at 1275°C under 75 V/cm [96].

Flash sintering was critically compared to Spark Plasma Sintering has been questioned. In the SPS method, the field is applied to a graphite die, therefore the majority of the current is passing through the die, and in some degree it passes through the depending on the material's conductivity. The applied electric fields are relatively low in SPS, however, current values reach as high as 100,000 Amperes which leads very high power density and high joule heating. On the other hand, in flash sintering, dc field is applied directly on the sample by two electrodes and all the current flow is through the sample. Another point is that flash sintering is a process low dc field, current is extremely low comparing to SPS method, and so is the power density imposed on system.

The reasons behind the anomalous enhancement of the mass transport flux in flash sintering is not fully understood yet. One wonders if flash sintering causes localized Joule heating at particle/particle contacts in the green body. Studies by Raj et al., however, clearly show that the increase in temperature due to transient power passing is not high enough to complete densification processes for flash sintering a wide range of material. Raj et al. demonstrated that the joule heating from the applied field in flash sintering obeys the Stefan Boltzmann law for black body radiation.

$$\frac{\Delta T}{T_0} = \frac{\Delta W}{4A\sigma T_0^4} \tag{2.5}$$

where T_0 is the specimen temperature without electric field, ΔW is the electrical energy (in Watt), A is the surface area of the specimen, and σ is a constant. Based on eq. (2.5), the typical $\Delta T = 0.01T_0$, which corresponds to only 1% increase in temperature. Hence, joule heating is not the root cause for flash sintering [99-102].

In the case of oxide ionic conductors, the electric is hypothesized to alter the defect because of electrostatic charge neutrality consideration. It is assumed that changed Frenkel pairs erected. These vacancies and interstitials are separated by electrostatic forces, and vacancies migrate toward grain boundaries, altering diffusional process thereby.

Following the discovery of flash sintering by Raj et al. in yttria stabilized zirconia (YSZ), the Rutgers group first focused on understanding of flash sintering mechanism in yttria stabilized zirconia using in-situ energy dispersive x-ray diffraction study to probe densification at the unit cell level. Yttria stabilized zirconia sample was heated with 9^{o}C/min heating rate, and x-ray data is collected with 1s intervals under 215 V/cm dc electric field up to 930^{o}C. Figure 2.15 shows the 2D topographic image of position dependence spectra along yr axis of the hot stage which is obtained at the X-17B1 beamline of National Synchrotron Light Source in the Brookhaven National Laboratory. The top and bottom spectra belong to insulator plates, and between insulator and the sample platinum electrodes are detectable with scan. Between insulator plates, the sample is seen with all major reflections of 8 % Y_2O_3-Z_rO_2 present.

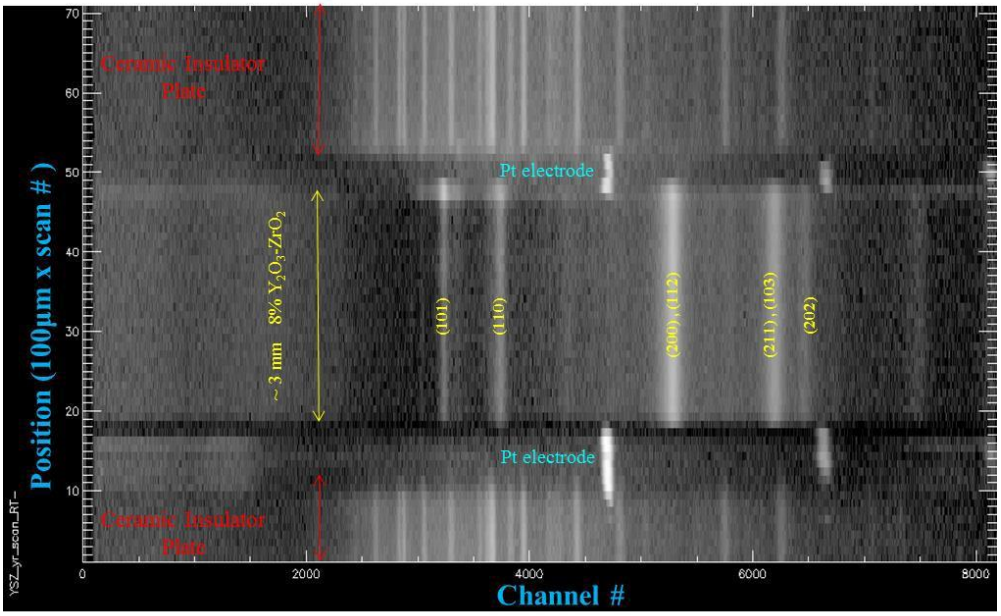

Figure 2. 15. Position dependence spectra, taken along yr axis of the hot stage [103].

Figure 2.16 shows variation of current as a function of time under 215 V/cm electric field. Current draw is observed at 876^{o}C and it reached to 3 A at 905^{o}C (power absorption ~513W/cm3) in 199 seconds. During this transient stage, YSZ powder is densified to 97% of the theoretical density.

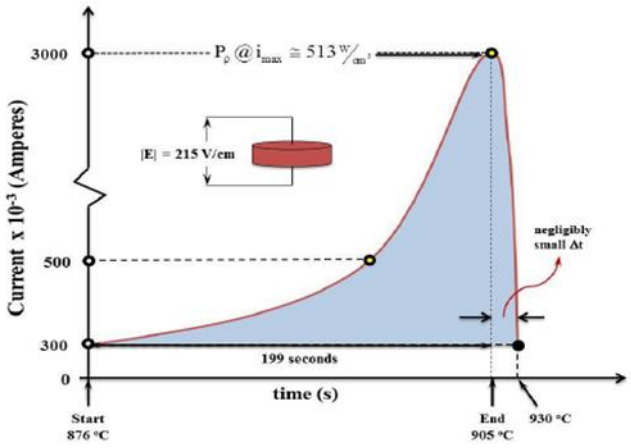

Figure 2. 16. Time dependence current draw by 8% Y_2O_3-ZrO_2 during flash sintering between 876 ^oC and 930 ^oC [104].

In Figure 2.17, the natural response of the unit cell volume of the tetragonal unit cell is depicted. Unit cell expands monotonously without current draw due to thermal expansion up to 876^{o}C. However, a current induced singularity is observed at 905^{o}C which corresponds to 2.35 % anelastic unit cell volume expansion. A second singularity at 847^{o}C is also seen which spontaneously and anelastically relaxes to thermal expansion baseline following an anelastic expansion.

Flash sintering of 8%YSZ has been performed under different dc electric field as well, and the effect of applied electric field on sintering temperature of YSZ is depicted in Fig. 2.18. The increase in the applied electric field during nonisothermal flash sintering experiments lower the sintering temperature of YSZ. The maximum observed current draw is 3 A when applied electric field is 183 V/cm at 841^{o}C which happens to be the optimum electric field strength for flash sintering of the YSZ [103,104].

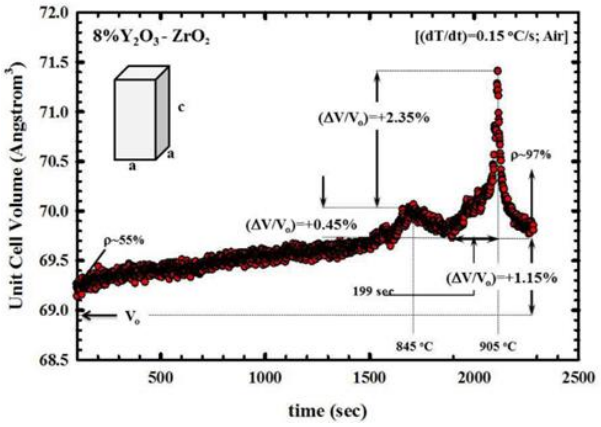

Figure 2. 17. Variation of the unit cell of 8% yttria stabilized zirconia as a function of time during flash sintering under 215 V/cm dc electric field [104].

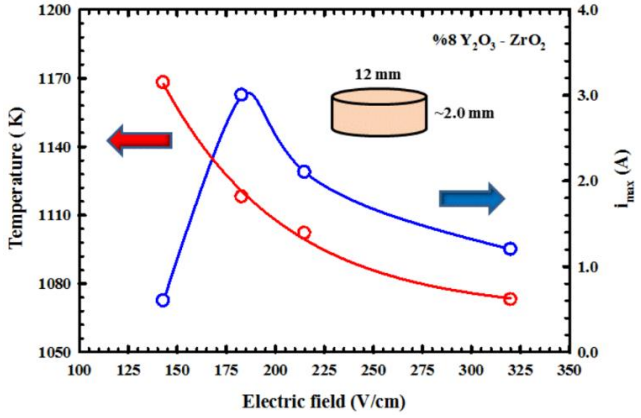

Figure 2. 18. Electric field effect on flash sintering temperature and current draw in yttria stabilized zirconia system (in review).

Figure 2.19 depicts the variation in the full width at half maximum of the representative (112) bragg reflection in YSZ as a function of time under 215 V/cm dc field. A singularity is observed at 980^{o}C that is indicative of defect process occurred at the point

of flash. During transient state, where current draw is observed and reach to 3 A, mass transport and defect process are coupled [104].

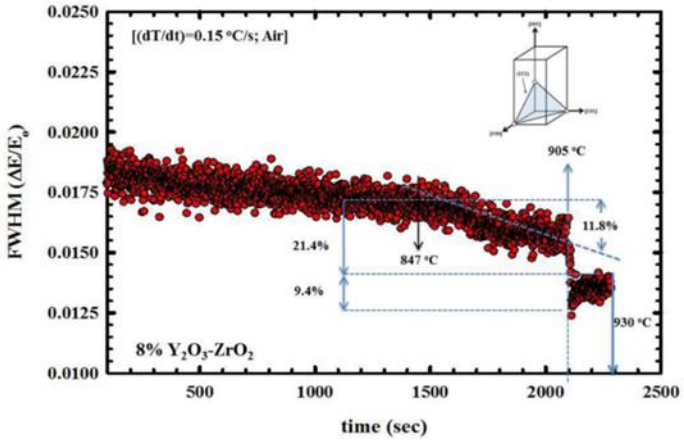

Figure 2. 19. The time dependence of full width at half maximum of the representative (112) bragg reflection in YSZ [104].

The flash process is overall provide energy reduction comparing to other sintering methods due to reducing sintering time and temperature. Basic furnace design and low power supply are sufficient to perform densification. Wide range of materials can be densified with this method, and specimen geometry is not limited to simple shapes. The flash sintering process is still under investigation, but it has great potential for industrial application in near future.

3. Thesis Objective

The primary goal of this study is to assess the possibility of densifying our ultrahigh melting temperature ceramic, B_4C, at low temperature to high density at the shortest time possible by Flash Sintering. Secondly, yet another main goal is to determine why

mass transport rates involved in the densification reach unprecedented level by what burst mode densification of B_4C in general.

3.1 Scope

The study presented herein covers in-situ experiments that were conducted in Brookhaven National Laboratory, Upton, NY where the purpose was to gain more insight into densification of B_4C at the unit cell level. For that purpose, high temperature energy dispersive x-ray diffractometry with an ultrahigh energy polychromatic synchrotron probe was used. Using this advanced analytical technique, the following tasks were accomplished:

3.1.1. Thermal Expansion of Boron Carbide as a function of E- field:

Thermal expansion is an anharmonic crystal property. By following the electric field dependence of the thermal expansion coefficient, we hope to gain insight into flash sintering phenomena at the unit cell level.

3.1.2. Densification of Boron Carbide and comparison of densification of B_4C under both isothermal and non-isothermal conditions:

Both isothermal and non-isothermal flash sintering experiments are performed to achieve densification of B_4C at low temperature and in a shortest time possible without grain growth. In so doing, one has the possibility to determine if the soret effect has a significant influence on flash sintering.

3.1.3. Comparison of densification of B_4C under different electric fields:

Sintering used in this study is recently discovered, a thorough analysis of the experimental parameters is carried out to assess the optimum condition for flash sintering of B_4C by burst mode densification. For that purpose in situ experimental work was performed at Brookhaven National Laboratory.

3.1.4. Characterization of Densified Sample:

While energy dispersive x-ray diffraction is the main tool of analysis in this study, other characterization techniques were also brought to bear to analyze sintered B_4C samples. Additional characterization studies include density measurement, microstructure examination, and angle dispersive x-ray diffraction. Comparison of the properties of B_4C that was densified with burst mode densification and conventionally sintered B_4C was also made.

4. Experimental Methods

4.1 Sample Preparation

This study is solely focuses on Boron Carbide (B_4C). The nano-particulated boron carbide powder with 50 nm median particle size was provided by Dr. C. Haines of Picatinny Arsenal, New Jersey. Powder did not require additional powder processing such as grinding, milling, etc. The as-received powder was uniaxially pressed into disk shaped body with diameter of 12 mm with a series of thicknesses from 1.5 mm to 3.5 mm. The high quality of powder enables us to press samples without binder, which was an advantage because the use of binder makes the densification more complicated due to

the arduous binder burn out process. The as-pressed densities of the specimen were 60-65 % of the theoretical density.

4.2. Parallel Capacitor Hot Stage for Field Assisted Densification Study

The furnace (hot stage) for in-situ flash sintering studies was custom made by Rutgers Nano-Materials group [136] exclusively for in-situ experiments at Brookhaven National Laboratory. As depicted in Fig. 4.1, the sample was placed between two spring loaded ceramics (insulator) made out of high temperature alumina (Al_2O_3) in all experiments. Resistance wire was wrapped around ceramic insulator, and connected to power supply (Power Designs Inc -Model 6150- Universal DC Power Source) to heat the specimen. The electric field was applied to the sample in the parallel plate geometry. Platinum foils were used as an electrode on both sides of the sample, and platinum wires were used to apply electric field. The power source (BK Precision -Model 9115- Multi Range DC Power Supply) which was used in boron carbide experiments was capable of delivering 1200 Watt and current limitation was set at 10 Amperes in all experiments. Temperature was measured with a thermocouple that was placed very carefully in the vicinity of sample (3-5mm). Voltage, current, and temperature data were recorded concomitantly with in-situ energy dispersive xrd experiments. An inert gas dynamic atmosphere (Ar) protected the specimen from oxidation.

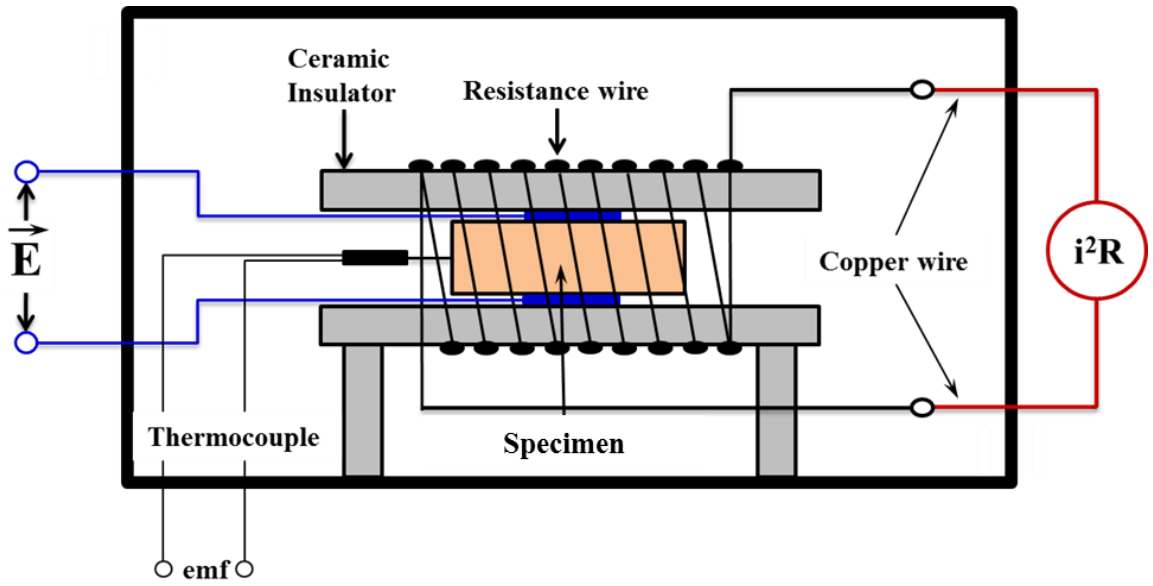

Figure 4. 1. Specialty hot stage designed and fabricated by the Rutgers Group for in situ analysis of Burst Mode Densification using ultrahigh energy dispersive x-ray diffraction [103, 136].

The hot stage was mounted on the sample positioning stage in the hutch of the X17-B1 beamline station as shown in Fig. 4.2., and exposed to beam with the Laue mode (transmission). Diffracted patterns were collected from body center of the sample by placing gauge volume (diffraction volume) on the body center after a delicate calibration procedure. The nominal heating rate was 25-40^{o}C per minute. Since the primary aim of this study is the discovery of boron carbide's response to flash sintering, non-isothermal experiments were conducted first. Several dc electric fields were applied on samples while heating and data was collected as will be discussed later. Once the temperature ranges of interest were obtained in nonisothermal experiments, isothermal experiments were also performed at different temperatures. The applied dc electric field was varied between 1-14 V/mm. X-ray data was collected every 2-3 seconds intervals from room

temperature to the sintering temperature as well as during cool down to room temperature.

4.3. Energy Dispersive X-ray Diffraction Method (EDXRD)

4.3.1. Preliminary considerations: Synchrotron Radiation

When charged particles are accelerated, electromagnetic radiation is produced. Electron or positron storage ring consists of an array of several magnets that keep charged particles on the radius path in a high vacuum pipe. When electrons pass through these magnets, they emit electromagnetic radiation x-ray tangentially to the plane of the orbit, and x-rays are directed along beamlines, and well-directed and intense x-rays are provided into the experimental areas. Simple image of storage ring (second-generation) is shown in Figure 4.2. Synchrotron radiation has very high intensity that is four to twelve orders of magnitude higher than conventional sources. Flux is determined with the number of photons per second; but for high intensity, the cross sectional size of the beam and distribution of the beam intensity as a function of wavelength should be taken into account. Any desirable wavelength (energies) can be chosen in synchrotron radiation due to high intensity from less than 1keV (1.4nm) to more than 70keV (~0.02nm), and experiments can be conducted with white radiation or any single wavelength by the use of monochromator. A conventional x-ray sources use few standard wavelengths with target materials of Cu-Kα (1.54184 Å) or Mo- Kα (0.71703 Å). Synchrotron radiation is highly collimated with fraction of miliradian, and produces very intense beam (high brightness and brilliance) and provide high resolution in diffraction study. Since synchrotron radiation is emitted when electrons pass through magnets, the radiation is

in pulses, not continues. These pulses can range in the picosecond to nanosecond depending on the properties of electron bunches in the storage ring. The acceleration of electrons leads radiation to be linearly polarized in the plane of the electron orbit [105,106].

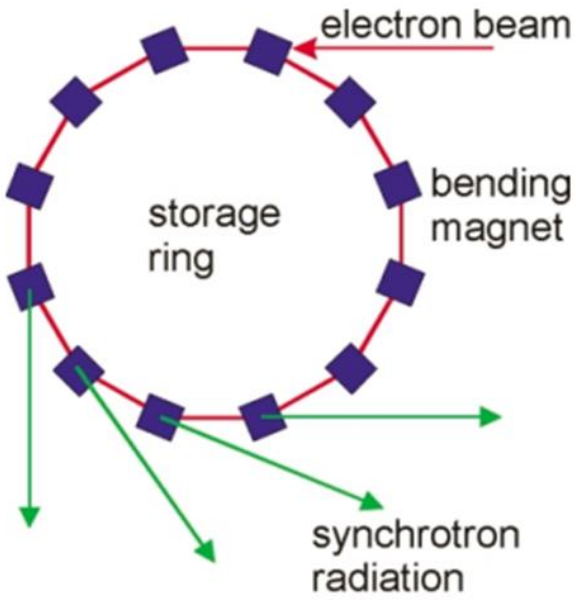

Figure 4. 2. Basic representation of a second-generation storage ring with output of synchrotron radiation from bending magnets [105].

4.3.2. Energy Dispersive X-ray Diffraction

In the energy dispersive x-ray diffraction (EDXRD) method, a diffraction pattern is obtained at a fixed Bragg angle (2-3^{o} typically) using a polychromatic X-rays from synchrotron. This is in contrast to Bragg-Brentano method where the diffraction is obtained at constant wavelength. Schematics of angle and energy dispersive x-ray diffraction methods are shown for comparison in Figure 4.3.

Multichannel solid state detectors allow simultaneous acquisition of whole diffraction in very short times thanks to the high brightness of synchrotron x-rays. This capability is especially important for high pressure in-situ experiments analyzing phase transition, sintering, chemical reactions, etc. Another important property of synchrotron EDXRD for in-situ experiments is the counting time which is at least one order of magnitude smaller than the ones associated with conventional method.

The EDXRD technique uses polychromatic radiation at fixed angle to fulfill the Bragg condition,

$$2d\sin\theta = n\lambda \tag{4.1}$$

The relation between the energy of a photon (E) and its frequency (ν) is given by the Planck-Einstein equation;

$$E = h\nu \tag{4.2}$$

where h is the Planck's constant, and for an electromagnetic waves, one has;

$$\nu = \frac{c}{\lambda} \tag{4.3}$$

where *c* is the speed of light in vacuum (2.997x10^8 m/s) and λ is the wavelength of the photon. If we combine equations (2.6), (2.7), and (2.8) one obtains;

$$d_{hkl}\sin\theta_{hkl} = \frac{6.199\ (\text{keV.Å})}{E_{hkl}} \tag{4.4}$$

In eq. (4.4), E_{hkl} is the measured quantity and hkl refer to the miller indices of the Bragg reflection of interest.

According to diffraction theory we have; $|\overrightarrow{Q_{hkl}}| = \frac{1}{d_{hkl}}$, where $\left|\overrightarrow{Q_{hkl}}\right|$ is the magnitude of the reciprocal lattice vector associated with the atomic plane (*hkl*). Therefore, $\left|\overrightarrow{Q_{hkl}}\right|$ is measured directly in an EDXRD experiment making it a very accurate method compared to angle dispersive x-ray diffraction where $d_{hkl} \propto sin^{-1}\theta_{hkl}$. Even small errors in the conversion of θ_{hkl} to sin $sin\theta_{hkl}$ results in large error in the calculation of d_{hkl} values due to the reciprocal relationship between d_{hkl} and θ_{hkl}. The EDXRD technique is a transmission mode (Laue) technique. One advantage of transmission mode is the elimination of the specimen height displacement errors that plague Bragg-Brentano methods. Also, the transmission mode enables strain field profiling/mapping of local strain field gradients in the materials with thicknesses of as high as 150 cm in aluminum, 2.54 cm in steel and 0.5 cm in tungsten.

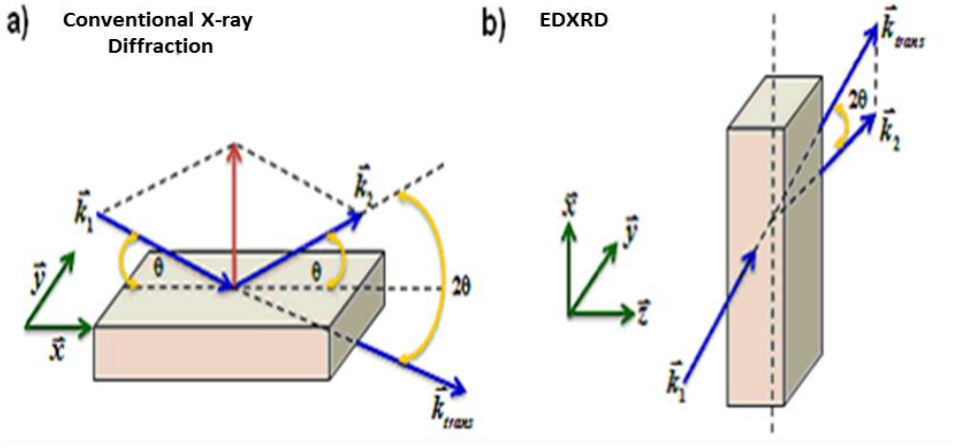

Figure 4. 3. Comparison of angle-dispersive and energy-dispersive diffraction [110].

Elastic strain can be measured at any given point in a 3D object of suitable thickness via,

$$\varepsilon_{hkl} = \left(\frac{\Delta d_{hkl}}{d_{hkl}} \right) = \frac{\Delta E_{hkl}}{E_{hkl}} \tag{4.5}$$

According to equation 4.5, the change in interplanar spacing or energy of given peak position can be measured as a shift in peak position on the energy scale in an EDXRD experiment. The elastic strain measurements can be computed under an applied stress in-situ. Moreover, with this technique, multi-phase system can be analyzed in a phase-specific manner with 1 second temporal resolution, and each phase can be identified separately. Therefore, EDXRD utilizing a synchrotron probe is ideal for micromechanics studies, for instance the effect of the applied stress on each component of the multi-phase system can be examined individually [107-114].

4.3.3. In-situ EDXRD analysis

In situ energy dispersive x-ray diffraction (EDXRD) measurements were performed in the National Synchrotron Light Source (NSLS) superconducting wiggler beam line X17-B1 in Brookhaven National Laboratory, Upton, New York. The experimental setup is illustrated schematically in Fig. 4.4. The photon (white beam) is produced by accelerating electron or proton to very high speed from which high energy x-rays are obtained (up to 200keV). A high resolution solid state Ge detector is used to collect spectra. The Ge detector is at liquid nitrogen cooled during measurements. In EDXRD technique, bragg angle is fixed to 2θ. The incident and diffracted beams from rhombic shaped gauge volume (GV) which is the diffraction volume. The GV is stationary and can be tuned by the incident and scattered beam collimating slits (2mm thick tantalum slits). The z dimension

of the GV (direction along the transmission) can be controlled by Bragg angle, hence, the higher the Bragg angle the shorter the GV. The following simple expression relates the gauge length (GL) to the slit opening, h and Bragg angle

$$tan(\theta) = \frac{2h}{L} \rightarrow L = \frac{2h}{tan(\theta)} \rightarrow L \ \alpha \ 1/\theta \qquad (4.6)$$

$$G_L = \frac{S_3}{sin2\theta} + \frac{S_1}{tan2\theta} \qquad (4.7)$$

where S_1 and S_3 are the slit openings in the x-y plane perpendicular to the z-axis. The S1 has horizontal and vertical components along the x and y axes of the Cartesian coordinate system. Hence, the shape of the S1 openings on the specimen's face is a rectangle whose dimensions can be adjusted as needed. The Bragg angle used in this study was typically $2\theta=3°$ which resulted in a gauge length of ~ 1 mm as the typical S1 y-axis opening used, i.e. 75 µm x 75 µm. (slit size). The slit opening determine the space resolution of the x-ray experiment. However, one needs to be extended to sample enough grains in a polycrystalline solid [113-119].

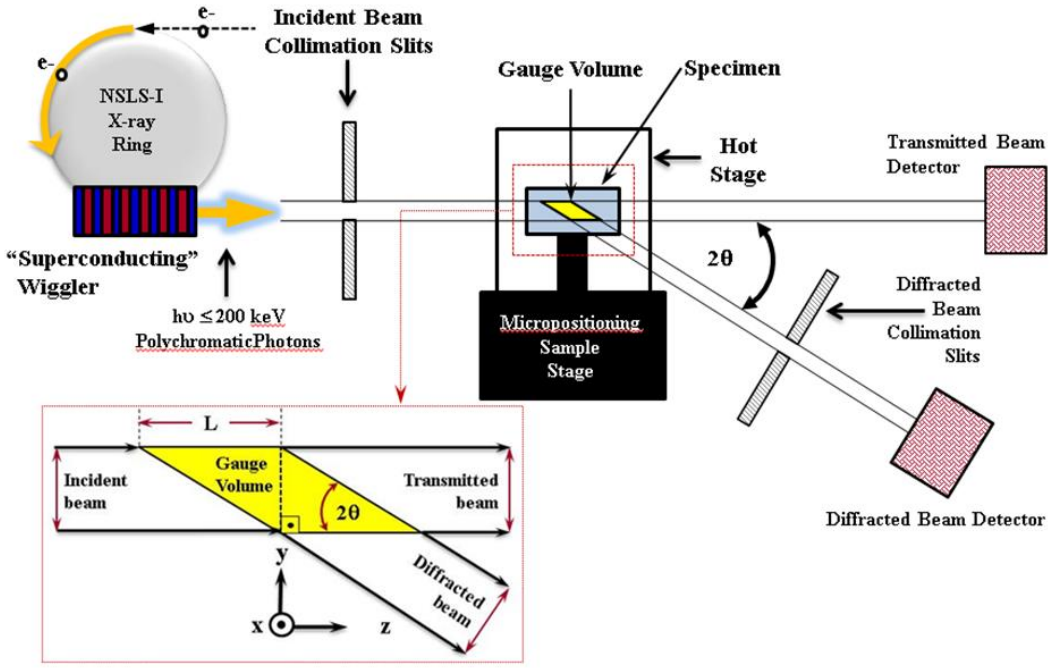

Figure 4. 4. Transmission (Laue) mode diffraction with a stationary diffraction volume in space makes the Rutgers approach very suitable for in-situ studies.

4.3.4. Energy Calibration and Data Analysis of Energy Dispersive X-ray Diffraction Technique

Energy calibration for the aforementioned EDXRD method was carried out with tungsten, gold, germanium, cerium oxide, and lanthanum hexaboride (LaB_6) (NIST SRM 660) standards. The spectrum of the LaB6 standard is shown in the Fig. 4.5

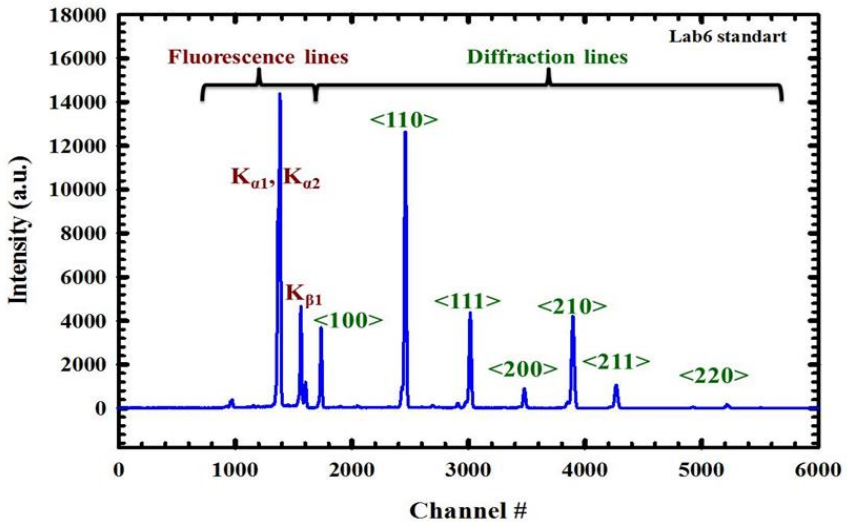

Figure 4. 5. The spectrum data of the LaB6 standard taken in the Rutgers EDXRD experiment [103].

Each channel number in the Germanium detector represents a certain energy point which then needs to be mapped on the known d-spacing of LaB_6 and other standards. The range of channel number was from 0-8192 corresponding to an energy range of 0-200 keV. $K\alpha_1$, $K\alpha_2$ and $K\beta_1$ lines of X-ray absorption (fluorescence lines) standards are used for calibration of the channel numbers against the energy scale up to ~40keV. For higher E CeO_2 and other standards are used. The instrumental broadening is ~1% which is dominated by the detector's contribution to the peak breath. It is measured as $\Delta E/E_o$, where ΔE is the width of the peak of interest at 50% of maximum intensity and E_o is the centroid coordinate of the peak. This instrumental error can be corrected with calibration using a LaB_6 standard.

Figure 4.6 displays a representative calibration result where a linear calibration curve which is obtained to map the measured channel numbers to the energy scale.

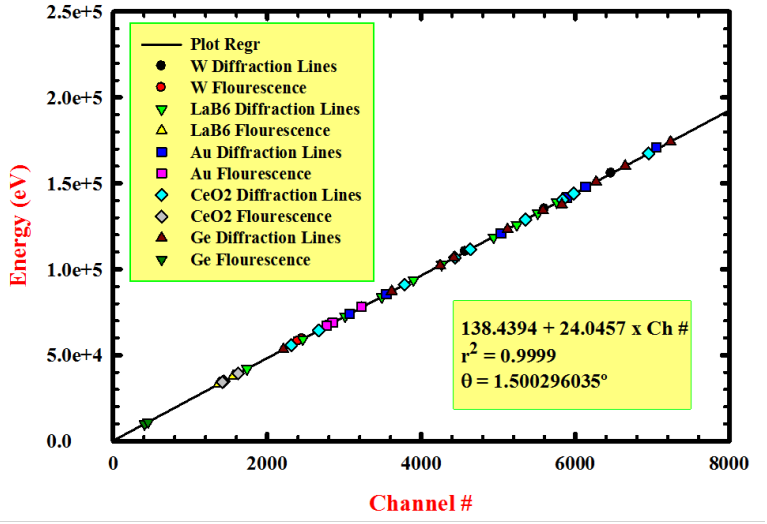

Figure 4. 6. Energy calibration result of the EDXRD set-up [103].

The final step in energy calibration is to obtain the governing equation for energy dispersive x-ray diffraction as,

$$d_{hkl} sin\theta = \frac{6.199\ (\text{keV.Å})}{E_{hkl}} \tag{4.8}$$

where d_{hkl} is interplanar spacing of the (hkl) reflection, θ is the bragg angle (2θ=3°), and E_{hkl} is the corresponding scattered energy from the (hkl) reflection which is measured quantity. Determination of the d_{hkl} values enables us to compute unit cell parameters of the rhombohedral cell boron carbide as a function of time, temperature, and electric field. All peaks from spectrum of B_4C were used to calculate lattice parameters. A non-linear least squares cell refinement program was used to determine hexagonal lattice parameters of boron carbide (a_H and c) from $d_{(012)}$, $d_{(003)}$, $d_{(101)}$, $d_{(021)}$, $d_{(104)}$, and $d_{(110)}$ reflections. Then, rhombohedral lattice parameters of B_4C (a_R, α) were computed by using the following equations,

$$a_R = \frac{1}{3}\sqrt{3a_H{}^2 + c^2} \tag{4.9}$$

$$\sin\frac{\alpha}{2} = \frac{3}{2\sqrt{3+(c/a_H)^2}} \tag{4.10}$$

$$V = a^3\sqrt{1-3\cos^2\alpha+2\cos^3\alpha} \tag{4.11}$$

The shift in peak position measured as a change in channel number, defines the volumetric unit cell variation as a function of time in the studies presented herein.

$$\frac{\Delta V}{V_0} = \frac{channel\ of\ \ peak - channel\ of\ \ peak_0}{channel\ of\ \ peak_0} \tag{4.12}$$

Channel of peak is the data taken from the sample under test and $channel\ of\ peak_0$ is the reference channel number. Moreover, the peak breadth is obtained by a profile shape function (pseudo-Voigt) from where defect process were monitored [113-119].

4.4. Other Characterization Techniques

4.4.1. Density Measurement

Densities of the as-sintered samples were measured with the Archimedes method. All samples were wiped with ethanol to remove surface residual prior to weighting, and dry weighted five time with Adam PGW analytical balance with 0.001g accuracy. Next, samples were suspended in a water, and weighted five times. The average of the

measured dry and suspended weights were taken, and density was calculated by using the following equation.

$$\rho\ (g/cm^3) = \frac{dry\ weight}{dry\ weight - suspended\ weight} \tag{4.13}$$

where the density of pure water was taken as 1 g/cm^3.

4.4.2. Scanning Electron Microscopy

The morphology of the powder particles and the microstructure of as-pressed, and as-sintered boron carbide samples were analyzed with scanning electron microscope. Zeiss Σigma field emission scanning electron microscope (FESEM) was used throughout this study.

All specimens were attached to an SEM stud with carbon tape. Powder was sprinkled on carbon tape and excess powder was removed with compressed air. No carbon or gold coating was issued since boron carbide samples were conductive. All samples were stored in a vacuum desiccator prior to use to eliminate moisture or contamination. Imaging was accomplished using secondary electrons and two detectors; a conventional secondary electron detector and an in-lens detector. The acceleration voltage range was 5V-20kV. Scanning was performed in the 1,000-20,000X magnification range to obtain the best results on boron carbide microstructure possible.

4.4.3. Qualitative and Quantitative X-ray Phase Analysis

As received nano boron carbide powders from each provider were examined with powder diffraction technique for phase purity. Measurements were performed with a Panalitical X'Pert X-Ray Diffractiometer. The powder mount (zero background) for Bragg-

Brentano was filled with boron carbide powder and powder was pressed with glass slide. Collected data from x-ray diffractometry was analyzed with the software, MDI Jade. Full pattern fitting was used for phase analysis.

5. Thermal Expansion Analysis

Thermal expansion is an important anharmonic material property for structural and mechanical applications as it is intimately related to the thermal stability and strength of the material. The thermal expansion coefficient (TEC) could be positive or negative under specified conditions but is usually positive. Most reported values for thermal expansion coefficients of materials are determined under constant pressure and zero electric field.

In general, thermal expansion can be defined with parameters; volume (V), temperature (T), and pressure (P) and V= f (T, P). The Pfaffian of V is

$$dV = \left(\frac{\partial V}{\partial T}\right)_P dT + \left(\frac{\partial V}{\partial P}\right)_T dP \tag{5.1}$$

and

$\alpha = \frac{1}{V_0}\left(\frac{\partial V}{\partial T}\right)_P$ is isobaric volumetric thermal expansion coefficient, and (5.1.1)

$\beta = -\frac{1}{V_0}\left(\frac{\partial V}{\partial P}\right)_T$ is isothermal (bulk) volume compressibility. (5.1.2)

If we substitute (5.1.1) and (5.1.2) into (5.1); then P-V-T equation of state becomes

$$dV(T,P) = \alpha V_0 dT - \beta V_0 dP \tag{5.2}$$

where α= f (T, P) and β= (T,P) in general.

Maxwell relation: $\left(\frac{\partial \alpha}{\partial P}\right)_T = -\left(\frac{\partial \beta}{\partial T}\right)_P$ (5.3)

Expand V into a maclaurin series around θ, where θ=298K

$$V(T) = V(\theta) + \left(\frac{\partial V(\theta)}{\partial T}\right)(T-\theta) + \frac{1}{2!}\left(\frac{\partial V(\theta)}{\partial T^2}\right)(T-\theta) + \ldots\ldots$$

$$\frac{\partial V(T)}{\partial T} = \left(\frac{\partial V(\theta)}{\partial T}\right) + \left(\frac{\partial^2 V(\theta)}{\partial T^2}\right)(T-\theta) + \ldots$$

$$\frac{1}{V(\theta)}\left(\frac{\partial V(T)}{\partial T}\right) = \frac{1}{V(\theta)}\left(\frac{\partial V(\theta)}{\partial T}\right) + \frac{1}{V(\theta)}\left(\frac{\partial^2 V(\theta)}{\partial T^2}\right)(T-\theta)$$

$$\alpha_V(T) = \alpha_V{}^0 + \alpha_V{}^{(1)}(T-\theta) + \ldots. \quad (5.4)$$

where $\alpha_V{}^0 = \left(\frac{\partial V(\theta)}{V(\theta)\partial T}\right)$ and $\alpha_V{}^{(1)} = \left(\frac{\partial^2 V(\theta)}{V(\theta)\partial T^2}\right)$ (5.5)

and per Binomial Theorem; $\alpha_L(T) = \frac{1}{3}\alpha_V(T)$

$$\alpha_L(T) = \frac{\alpha_V{}^0}{3} + \frac{\alpha_V{}^{(1)}}{3}(T-\theta) + \ldots. \quad (5.6)$$

Thermal expansion behavior of boron carbide has been reported in several articles. Average thermal expansion coefficient in the 298-1073 K temperature range is reported 4-8 10^{-6} K^{-1} in the Thevenot's review paper, and Pilladi reported that average thermal expansion coefficients in the 298-1773 K temperature range for nano and microcrystalline boron carbides are 7.76x10^{-6} K^{-1} and 7.06x10^{-6} K^{-1}, respectively [10,14]. In this study, we used the advantage of in-situ flash sintering experiments conducted at NSLS, BNL to determine thermal expansion coefficient of boron carbide under different electric field strength. Data collection from body center of the sample enable us to

measure unit cell parameters while heating the sample under a constant electric field. Advantages of the x-ray method over classical measurements of thermal expansions as follows; the measurement excludes the effect of the impurity on thermal expansion in the sample by measuring directly the unit cell variation of the material, specimen size is not important, and single experiment is enough to determine the thermal expansion coefficient of material [121-123].

5.1 Experimental

Nanocrystalline boron carbide samples have been analyzed in X-17B, NSLS, Brookhaven National Laboratory. Experimental setup is explained in Section 4. Bragg angle of 2θ value was set at 3^{o}. Electric field is varied between 0.0 V/mm to 12.73 V/mm for nanocyrstalline B_4C samples. Data is collected every 2-3 seconds that yields overall more than 1000 spectra for each experiments, but diffractions belong to specific temperatures are chosen for final determination of thermal expansion coefficients. Temperature range differentiates for each measurement from room temperature to up to $1010^{o}K$. Thermal expansion was measured in the absence of electric field as a baseline with temperature interval of ~100K. Experiments are performed at 0.0 V/mm, 5.3 V/mm, 6.9 V/mm, and 12.7 V/mm for nano-boron carbide samples with the temperature range from room temperature to $1010^{o}K$, $875^{o}K$, $730^{o}K$, and $615^{o}K$, respectively.

Lattice parameters of boron carbide were computed accurately with UnitCell software which is used to refine hexagonal cell parameters for boron carbide by using all six peaks [(101),(003),(012),(110),(104), and(021)] in the spectrum data. Pre-estimation

of lattice parameter is not necessary for UnitCell program which uses non-linear least-squares method [121].

5.2. Results

Figure 5.1 shows the room temperature (298K) energy dispersive x-ray diffraction (EDXRD) pattern of the as-received nanocrystalline boron carbide powder as a function of Energy (keV) for $2\theta=3^{o}$. The room temperature lattice parameters of boron carbide are a_R=5.1684 Å and $\alpha_R=65.7046^{o}$ that are obtained from EDXRD spectrum. The as-received powder was also assessed by quantitative x-ray phase analysis using whole pattern fitting of Bragg-Brentano diffraction spectrum (Fig. 5.2). Whole pattern fitting phase analysis indicated that 2.1 % free carbon was present in the as-received powder. Chemical analysis of the boron carbide that is used in this study is shown in Table 5.1.

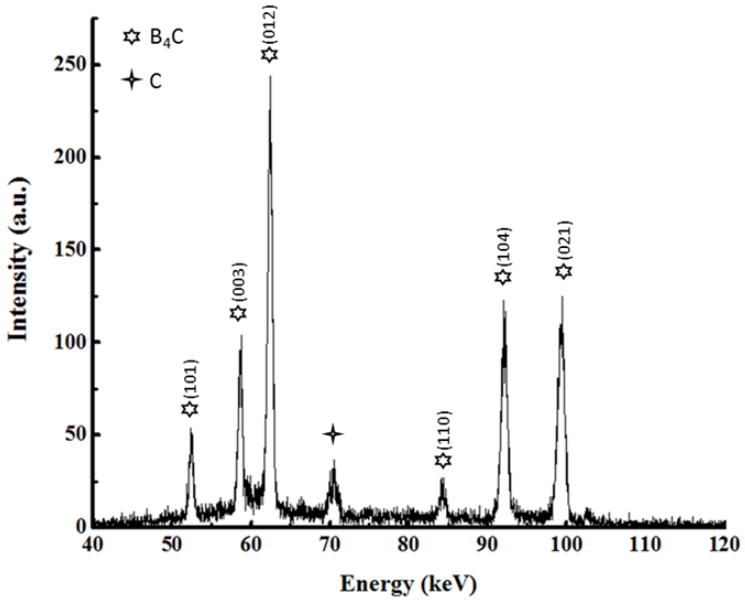

Figure 5. 1. The energy dispersive x-ray diffraction spectra of as-received boron carbide at room temperature (298K) as a function of channel number.

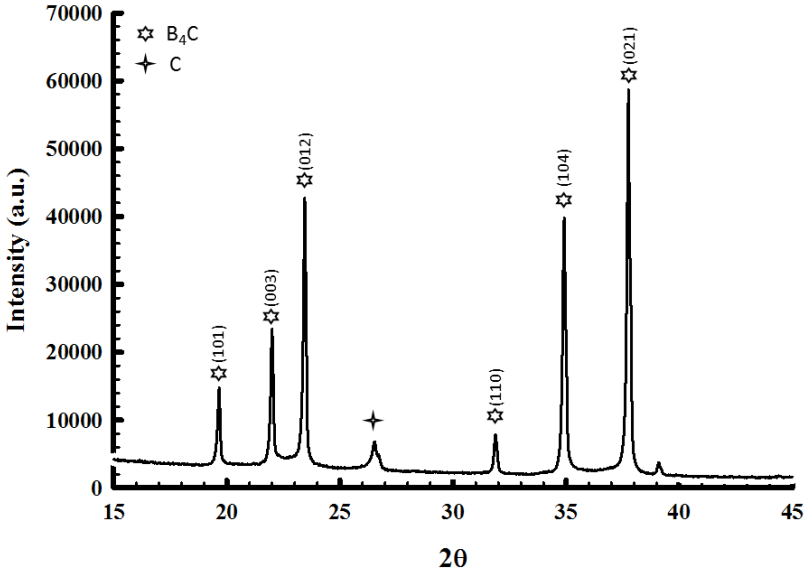

Figure 5. 2. Bragg-Brentano diffraction spectrum of as-received B_4C powder.

Table 5. 1. Chemical analysis of nanocrystalline boron carbide presented in this study

Sample name	Boron (wt.%)	Carbon (wt.%)	Phases present in XRD analysis
N-B_4C	74.7	25.3	B_4C and C

Figure 5.3 depicts the variation of the rhombohedral unit cell parameter of nano-B_4C as a function of temperature (K) under various applied dc electric fields. Lattice parameter (a_R) increases monotonously while temperature increases. The variation is parabolic and not linear despite the fact that the temperature range of interest is < T_m. The TEC was found to exhibit E-field dependence as well as can be also verified in Fig. 5.3. The variation of the lattice parameter with temperature becomes more nonlinear as the electric field strength is increasing.

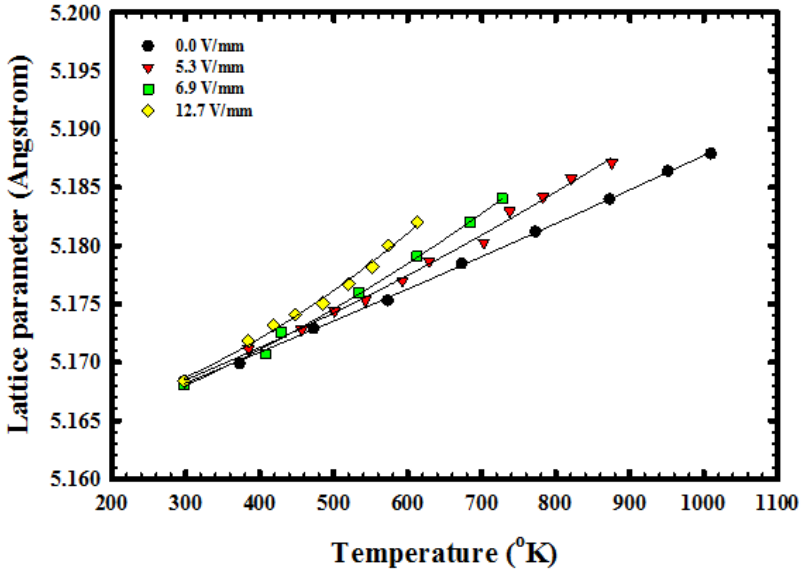

Figure 5. 3. The variation of rhombohedral B_4C unit cell parameter, a (Å), as a function of temperature (K) under various applied dc electric field (V/mm).

On the other hand, the rhombohedral angle of B_4C is invariant and only fluctuates with respect to a temperature increase and the applied field has no effect whatsoever. As seen in figure 5.4, this invariance suggests that the expansion of unit cell of B_4C is hydrostatic with increasing temperature.

The variation of the unit cell volume of the rhombohedral B_4C is shown in Figure 5.5. The effect of the applied electric field is same as discussed for lattice parameter (a_R) of B_4C, and with increase of electric field, the dependence of unit cell volume on temperature becomes more non-linear.

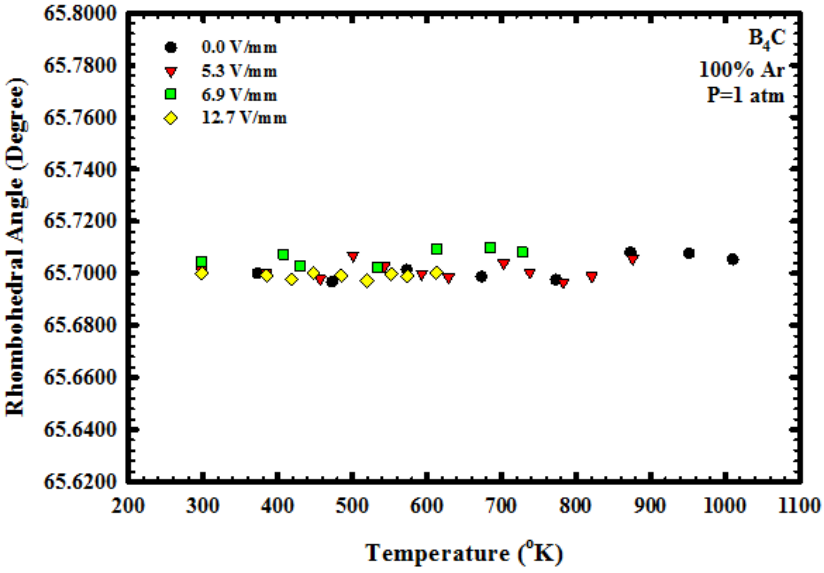

Figure 5. 4. The variation of the rhombohedral angle (α) of B_4C as a function of temperature (K) under various applied dc electric field (V/mm).

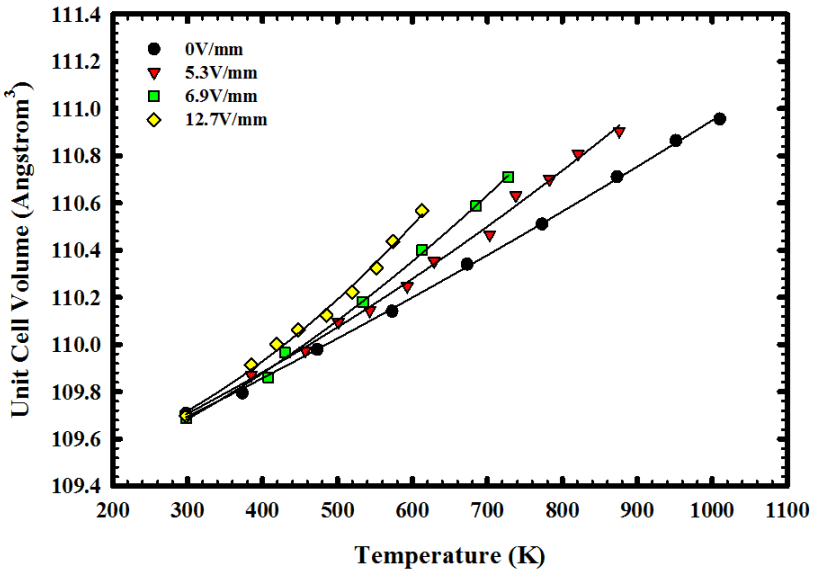

Figure 5. 5. The variation of the unit cell volume of the rhombohedral B_4C as a function of applied electric field.

Quadratic fitting of lattice parameter versus temperature (K) data (in Fig. 5.3) reveals following equation for each specimen;

0.0 V/mm (298K-1010K); $a_T = 5.1684 + 2.492\times10^{-5}(T-298) + 3.778\times10^{-9}(T-298)^2$ (5.7)

5.3V/mm (298K-875K); $a_T = 5.1684 + 12.663\times10^{-5}(T-298) + 1.131\times10^{-8}(T-298)^2$ (5.8)

6.9 V/mm (298K-730K); $a_T = 5.1684 + 2.758\times10^{-5}(T-298) + 1.992\times10^{-8}(T-298)^2$ (5.9)

12.7 V/mm (298K-615K); $a_T = 5.1684 + 3.195\times10^{-5}(T-298) + 3.277\times10^{-8}(T-298)^2$ (5.10)

The equations (5.7-5.10) can be written as; $a_T = a_0 + A\Delta T + B\Delta T^2$, so the first and second coefficients of thermal expansion will be $\alpha_L^{(1)} = \frac{A}{a_0}$ (K^{-1}) and $\alpha_L^{(2)} = \frac{B}{a_0}$ (K^{-2}), respectively. The variation of the $\alpha_L^{(1)} = \frac{A}{a_0}$ and $\alpha_L^{(2)} = \frac{B}{a_0}$ as a function of applied E-field are depicted in Fig. 5.6, and as seen from the graph, the increase of the electric field strength on material will increase the first and second coefficients of thermal expansion of B_4C.

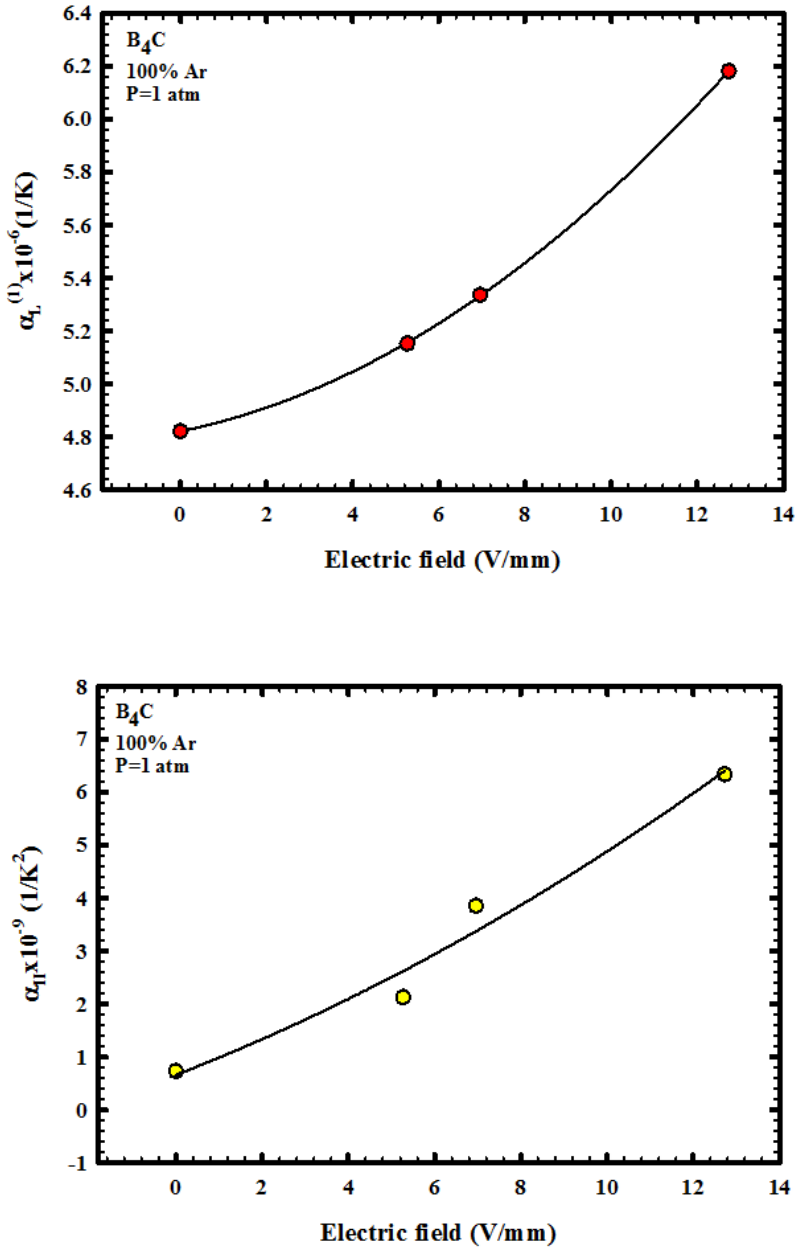

Figure 5. 6. The variation of the first (top) and second (bottom) coefficient from data points of lattice parameter versus temperature under different dc field.

The first ($\alpha_L^{(1)}$) and second ($\alpha_L^{(2)}$)thermal expansion coefficients as a function of applied electric field is also fitted to second degree polynomial (Fig. 5.6) that give the

relation between electric field and thermal expansion coefficients that are presented in Table 5.2 and with equations below;

$$\alpha'(T,E) = \alpha^{(1)}{}_T\,(T)_{E=0} + \varphi_1\left(E - E_0\right) + \varphi_2\left(E - E_0\right)^2 \quad (5.11)$$

$$\alpha''(T,E) = \alpha^{(2)}{}_T\,(T)_{E=0} + \zeta_1\left(E - E_0\right) + \zeta_2\left(E - E_0\right)^2 \quad (5.12)$$

Table 5. 2. The relation between thermal expansion coefficients of B_4C and electric field strength in which thermal expansion measurements were performed.

	α(T) E=0	**Coeff. 1**	**Coeff. 2**
α^{I} (T,E)	4.821×10^{-6}	3.30×10^{-8}	5.8×10^{-9}
α^{II} (T,E)	6.653×10^{-10}	3.24×10^{-10}	9.87×10^{-12}

5.3. Discussion and Conclusion

In-situ energy dispersive x-ray diffraction study on lattice parameter of boron carbide under various electric field while heating the specimen shows that the lattice parameter a_R increase monotonically with temperature while α_R remains unchanged. For polycrystalline materials the grain orientation is random. Although individual grains behave anisotropically, the property differences tend to average out and at larger scale polycrystalline material will be approximately isotropic.

The linear thermal expansion coefficient for N-B_4C is 4.821×10^{-6} at $\vec{E} = 0$ which is in reasonable agreement with the value reported in the literature. Moreover, we have shown that the application of the electric field across the sample in the parallel plate capacitor geometry while heating the sample has impact on the thermal expansion coefficients of the material. If we increase the electric field strength on the sample, the first and second thermal expansion coefficients of boron carbide gain higher values, and

such relation was shown with quadratic regression of the lattice parameter versus temperature (K) data. While temperature affects the anharmonicity of the lattice interaction potential by itself, conjugated effect of the thermal and electric field have higher impact on interatomic separation. The impact of the superimposed thermal and electric field on thermal expansion coefficients of boron carbide was determined by the quadratic fitting of the thermal expansion coefficient versus the electric field data. Such non-linear behavior reveals two separate coefficients for the correlation between applied dc field and the coefficients of thermal expansion as summarized in Table 5.2. The results shown here are fundamental data for boron carbide, which is used in applications varies from structural to electronics. Moreover, the effect of the applied electric field on material while heating could be necessary to put more insight for flash sintering processing for the material system of interest.

6. Densification of Boron Carbide under Superimposed Thermal and Electric Field

Highly covalent bonded ceramics have low diffusivity and require high temperatures, long time, and pressure assistance to obtain full densifications as discussed earlier. Electric field assisted densification processes are studied to enhance densification by providing driving force to induce nucleation and densification in such ceramic systems [68, 102, 124, 125].

In this chapter, we demonstrate the first experimental study for densification of boron carbide specimen under electric field strength while heating the specimen with constant heating rate.

6.1. Experimental

Nano boron carbon powder (~100nm) was pressed into ~2.5 mm thickness. The specimen was sintered in a flowing argon gas atmosphere at 1 atmosphere by heating them with 30 ^{o}C/min rate under 4.5 V/mm. The limiting current was set 10A in the beginning of the experiment. The in situ synchrotron x-ray diffraction was performed with a fixed Bragg angle of $2\theta=3^{o}$. The specimen was heated under electric field while diffraction from full x-ray spectra was collected in the Laue mode every 2 second. All observed Bragg reflections were fitted with a pseudo-Voigt profile shape function (pV PSF). Experimental details can be found in Section 4 and see Appendix 1 for methodology of current-induced enthalpy increment.

6.2. Results

The variation of electrical power density absorbed by B_4C under 4.5 V/mm constant dc field as a function of time was shown in Figure 6.1 (data shown from 850 s onwards for illustration purposes). The sample was convectively heated with ~30 ^{o}C/min heating rate from room temperature (t_0=0) to 711 ^{o}C (t=1324 s). Firstly, up to 501^{o}C (ambient temperature) an incubation period of 1000 seconds is observed during which the current drawn by B_4C remained well below 0.1 A. Secondly, the spontaneous current draw reached 0.74 A during a linear onset stage which is observed from 501^{o}C to 688^{o}C. Thirdly, between 688 and 711 ^{o}C, a spontaneous rapid rise in current from 0.74 to 10 A is observed. Once the current hit its maximum value of 10A, the voltage started to decrease because of the reduction in resistivity of specimen while it sinters, and system eventually

reached to steady state where current and voltage remain constant. At this point, we shut down the power source to eliminate possible joule heating causing by the steady state.

The maximum peak power density absorbed by B_4C specimen was ~350 W/cm^3 at 711 ^oC and 10 A. The third range, transient power pass through the specimen only takes place in 28 seconds, resulting in an increase in density from 65 to 95% of the x-ray density.

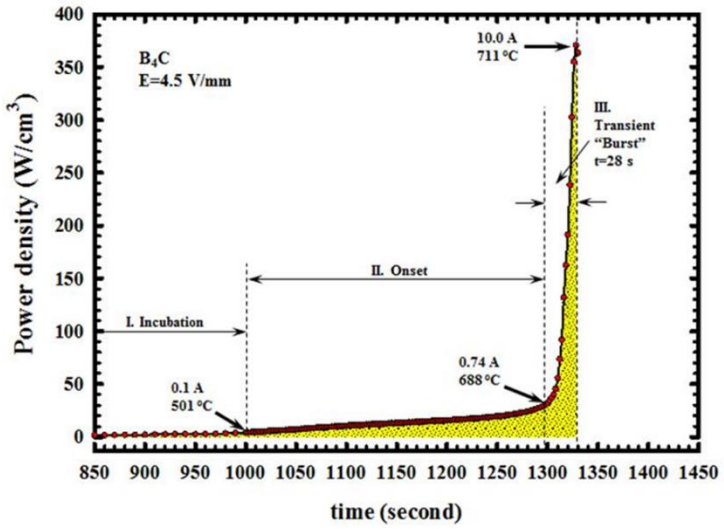

Figure 6. 1. The time evolution of electrical power absorption density in the sintering of B_4C with 4.5 V/mm in 1 atm pure argon atmosphere.

Figure 6.2 shows a scanning electron micrograph (SEM) of a pristine fracture surface in a 95% dense B_4C obtained in this study. A grain size of ~100 nm is observed as seen in figure, indicating that no grain growth occurred since the initial powder particle size is commensurate with the final grain size of the ceramic.

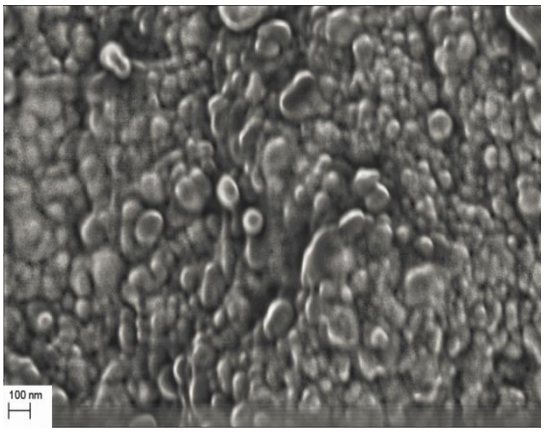

Figure 6. 2. The field emission scanning electron micrographs of pristine fracture surfaces of sintered B_4C by Burst Mode Densification

We have carried out *in situ* energy dispersive x-ray diffraction to provide explanation for the evolution of densification in boron carbide at unit cell scale. Therefore, we were able to observe the current-induced changes in the B_4C unit cell with Δt = 2seconds during flash sintering under 4.5 V/mm. Figure 6.3 depicts the variation of B_4C unit cell volume with time under a 4.5 V/mm constant electric field. When we also add the current variation with time on the same graph, it is remarkably noticed that the B_4C unit cell volume follows the identical 3-stage temporal evolution that was observed in the macroscopic variation of power density with time (See Fig. 6.1). There is a monotonous unit cell expansion over the incubation period (Stage I) as the current flow through the B_4C lattice is less than 0.1A by basically following thermal expansion coefficient. The B_4C unit cell expands faster from 501-688 ^oC and the expansion shows 0.9% increase when the spontaneous current draw increased from 0.1 to 0.74 A in 296 seconds. In the third stage, where the transient current flow through specimen was observed, the B_4C unit cell undergoes an anomalous very large expansion of 1.12%. During Stage III, the current increases from 0.74 A (688 ^oC) to 10.0 A (711 ^oC) in only 28 seconds.

The cumulative unit cell expansion which is corresponded to stages II and III is a 2.02%. For t >1324 s nonisothermal anelastic relaxation is observed even though the heating continues as the decrease in B_4C unit cell volume is time dependent [129].

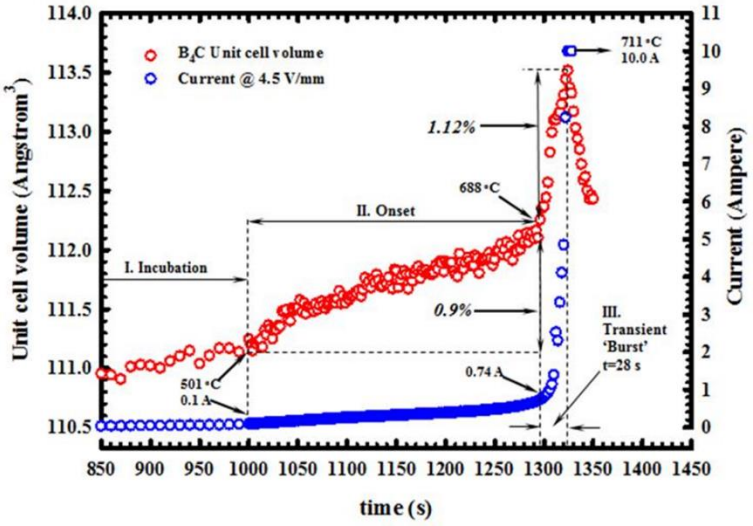

Figure 6. 3. The current-induced unit cell expansion in rhombohedral B_4C as a function of time and current.

Figure 6.4 shows that the rhombohedral angle of B_4C is not subject to change with time and also shows no dependence on current. The current driven unit cell expansion of boron carbide is isotropic due to invariance of the unit cell shape while it expands, and it exhibits spherical symmetry (Curie group $\infty\infty$m) [130]. Furthermore, Figure 6.5 reveals that there is no discontinuity in full width at half maximum (FWHM) of the Bragg peaks as a function of current during transient state (exemplified here by the FWHM of (021) and (003) reflections), which is in complete contrast to what was observed in the yttria stabilized zirconia system. In zirconia, current driven unit cell expansion is due to migration of point defects, however, such invariance in FWHM for B_4C confirmed that the

current-driven unit cell expansion is solely due to the burst of small polarons through the B_4C lattice. Only a slight decrease with increasing time in the FWHM vs time traces were seen under 4.5 V/mm during overall experiment due to densification [131].

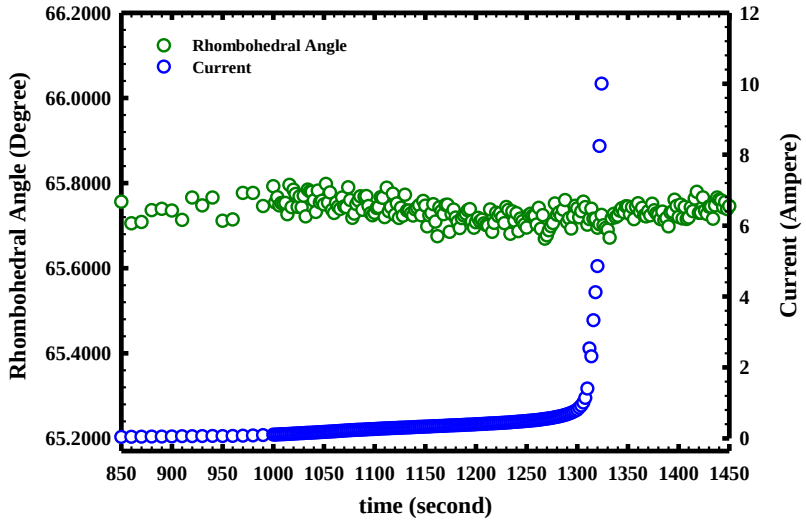

Figure 6. 4. The time dependence of rhombohedral angle (α) of B4C unit cell.

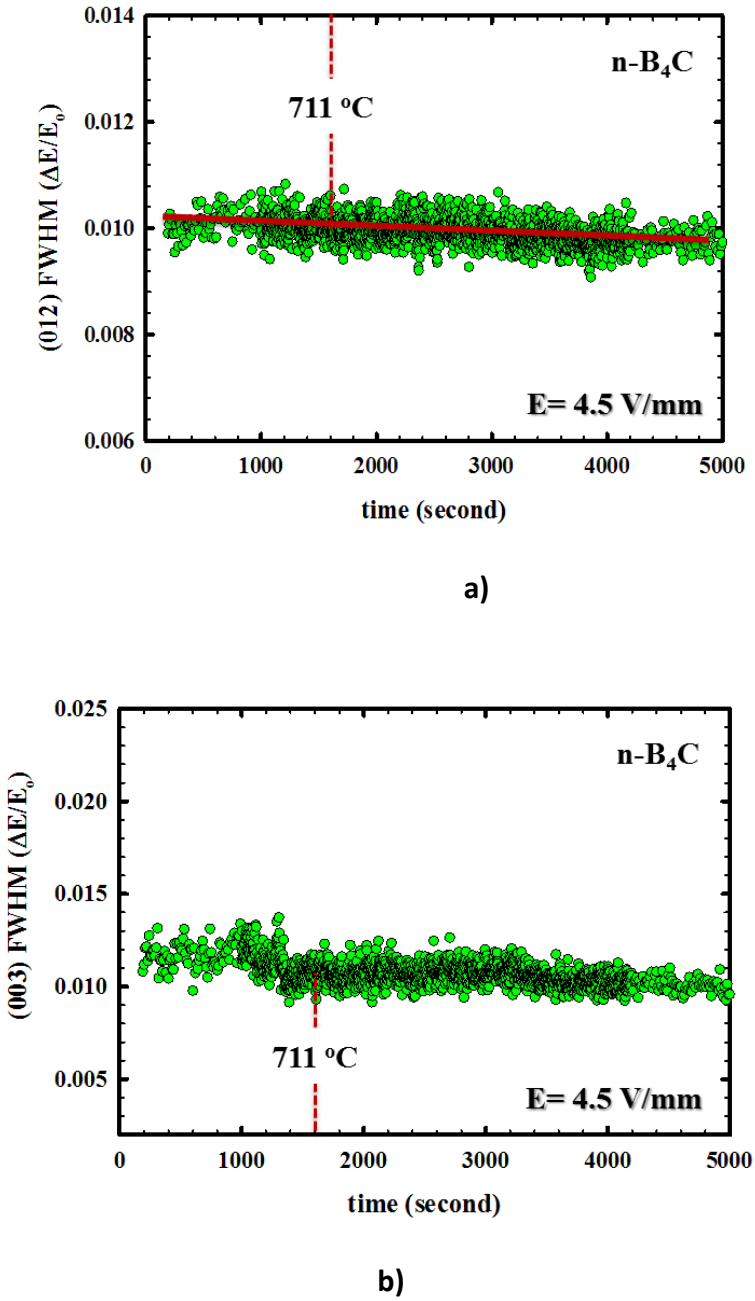

Figure 6. 5. The time dependence of full width at half maximum (FWHM) of the representative a) (012) and b) (003) Bragg reflections.

6.3. Discussion and Conclusion

When one works on flash sintering, one question immediately comes to mind: the contribution of Joule Heating, especially during transient state (Stage III). Our approach for investigation of the input of Joule heating to observed fast atomic transport rates was relied on assumption that electrical energy was absorbed by B_4C from 0.74 A (688^oC) to 10A (711^oC) adiabatically. Power-time relation of B_4C (Fig. 6.1) was integrated and the enthalpy increment was calculated by using thermodynamic data of B_4C as described in Appendix 1. The current-induced enthalpy increment was found as ΔH(J)=89.5 kJ/mol for Stage III. The enthalpy increment accompanying with thermal field is ΔH(T)= 85 kJ/mol between 25-711 ^oC. Combination of thermal and current induced enthalpy increment results $\Delta H^o(T,J)$=174.5 kJ/mol which is corresponded to 1312^oC, adiabatic internal temperature of B_4C. Such internal temperature is not sufficient for the observed colossal unit cell expansion and thermally activated mass transport in just 28 seconds. Moreover, we performed basic calculation of required temperature rise to reach the observed unit cell expansion in Stage III by using thermal expansion coefficient of B_4C in the absent of electric field;

$$\alpha_L^{n-B_4C} = 4.82\times10^{-6}\ {}^oC^{-1} \Rightarrow \alpha_V^{n-B_4C} \simeq 3\alpha_L^{B_4C}$$

$$\Rightarrow \alpha_V^{n-B_4C} \simeq 14.46\times10^{-6}\ {}^oC^{-1}.$$

$$\varepsilon_V^{n-B_4C} = 1.12\% \quad \textit{(transient stage)}$$

$$\varepsilon_V^{n-B_4C} = 14.46\times10^{-6}\ {}^oC^{-1}\Delta T^* \Rightarrow \Delta T^* \simeq 775\ {}^oC$$

$$\Delta T^{Exp} \simeq 23\ {}^oC \Rightarrow \Delta T^{Exp} \neq \Delta T^*$$

The above result also shows that joule heating cannot be solely the cause of observed colossal unit cell expansion in Stage III with Δt=28 seconds.

Boron carbide is not an ionic conductor, therefore there is no direct coupling between electric field and mass transport via electrochemical potential. Also, B_4C does not present magnetoelectricity and magnetoristriction causing by the coupling mechanism between electric field and elastic strain. The current driven unit cell expansion in B_4C is due to small polaron transport through rhombohedral lattice, and such transport is thermokinetic phenomenon. We name this new direct coupling mechanism between electric current and unit cell volume the galvanomechanical effect (GME). Moreover, there is a correlation between current driven unit cell expansion and the diffusivity of rate limiting species in B_4C during transient range considering most of the densification occurs during Stage III. Therefore, it is concluded that the current driven unit cell expansion induces the densification of B_4C. From first principles based on random walk theory, the diffusivity of a species (D_i) in a crystal lattice depends on the unit cell parameter (a) of the host as $D_i \sim a^2$, which results in a unit cell volume (V) dependence of $D_i \sim V^{2/3}$. In Stage III, regression analysis to the temporal time evolution of unit cell volume (Fig. 6.3) shows $V \sim t^3$ dependence, and a parabolic time dependence of diffusivity, $D_i \sim t^2$[133-135]. The observed density increase in 28 seconds in Stage III can be explained approximately with a~800% increase in diffusivity of the rate limiting species in B_4C.

Due to the reduction in sintering temperature and time, flash sintering of high temperature ceramics promises potential energy saving in the sintering process.

7. The Investigation of the Effect of Different Flash Sintering Conditions on Densification of B_4C

In the previous chapter, we analyzed the feasibility of flash sintering of B_4C by using particular example under 4.5 V/mm nonisothermally. Flash sintering is a new method which requires extensive research for optimization of process variables to obtain full density and best mechanical properties. For this reason, we have conducted several in-situ flash sintering experiments both isothermally and nonisothermally under different electric fields. In the first section of this chapter, the discussion on the effect of the sintering condition will be presented by showing the results of non-isothermal and isothermal experiments. In the second part, the effect of the application of different electric field under nonisothermal condition will be discussed.

7.1. Isothermal and Nonisothermal Flash Sintering of B_4C under Similar Electric Field

Flash sintering of boron carbide was performed under nonisothermal and isothermal conditions at both Rutgers and NSLS, BNL. Upon successfully densification of nano particulate B_4C specimen at 880^{o}C non-isothermally with the application of constant electric field of 3.8 V/mm, isothermal experiment was designed at 870 ^{o}C with similar electric field (3.6 V/mm) on identical sample to define the influence of temperature in sintering process. The experimental procedure is same as previous section except for specified dc fields and temperatures during chapter. In addition to the knowledge of the temperature at which power rises for aforementioned e-field, similarity of experimental parameters between isothermal and non-isothermal experiments (such as applied

electric field, heating rate, and current limitation) promotes understanding of burst/onset time duration and unit cell response to current change in a manner.

7.1.1. Results

Figure 7.1 depicts the power density absorption by B_4C for nonisothermal and isothermal flash sintering conditions under applied field of 3.8 V/mm and 3.6 V/mm, respectively; here the data starting time is set to 0sec at beginning of the current draw for comparison purpose. Power density variation under a constant electric field of 3.8 V/mm while heating with 30^{o}C/min heating rate does not show any current draw from room temperature to 770^{o}C. From 770^{o}C to 863^{o}C the current monotonically and spontaneously increases from 0.1A to 1 A in 151 seconds. The third range which is also called as 'transient burst' depicts the spontaneous rapid rise in current draw from 1 A to 10 A in just 12 seconds. The maximum absorbed power density is ~334 W/cm^3 at 880^{o}C. The temperature increase during transient burst is very low and is from 863^{o}C to 880^{o}C only. In the isothermal experiment, 3.6 V/mm electric field is applied instantaneously at 870^{o}C and current draw reached 0.1A as soon as the electric field is applied; see Figure 7.1. Onset time between 0.1 A to 1 A is 288 seconds during which no significant temperature increase is observed (ΔT 5^{o}C). The peak power density reached to ~320 Watt/cm^3 in just 21 seconds based on transient burst between 1A to 10A. Observed transient stage caused the increase of the temperature from 875 to 896.7 ^{o}C. In both experiments, once 10 A is reached, the power supply was switched from voltage control to current control (not shown in Fig. 7.1). In other words, the electric field was decreased since the resistivity of the sample decreases with increasing temperature. The current

control stage is the steady state range over which Joule heating is expected to occur. Therefore, power source was switched off to prevent joule heating. The data in hand suggest that there is no major difference in burst mode between isothermal and nonisothermal conditions, and maximum absorbed power density was similar in both case.

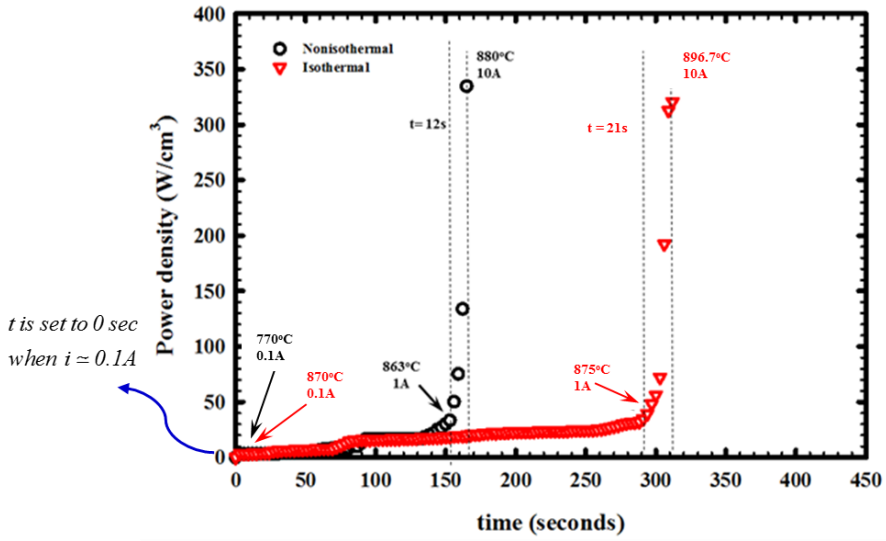

Figure 7. 1. The comparison of absorption of power density by B_4C samples between nonisothermal and isothermal flash sintering conditions.

Here (Fig. 7.1), one observes that the onset time from 0.1 to 10A is longer for isothermal condition even though applied electric field is approximately the same in both experiment. Moreover, the transient state also occurs faster under nonisothermal condition than the one under isothermal condition. The temperature increase during the transient state for nonisothermal and isothermal conditions are 17°C and 21.7°C, respectively. Such a difference is the result of a longer transient state in the isothermal process causing higher power absorption by the material leading to increase in

temperature by joule heating. The current induced energy absorption for both experiment and for two regions (onset stage and transient stage) are found by integrating the data from Fig. 7.1 as follows;

Non isothermal condition with 3.8V/mm;

$$W(t) = \int_{t_1=0}^{t_2=165} P(t)dt \Rightarrow W(\Delta t) = 1245.54\ J \ \rightarrow\ 68.72\ kJ/mole. \tag{7.1}$$

$$W(t) = \int_{t_1=153}^{t_2=165} P(t)dt \Rightarrow W(\Delta t) = 526.5\ J \ \rightarrow\ 29.5\ kJ/mole. \tag{7.2}$$

Isothermal condition with 3.6 V/mm;

$$W(t) = \int_{t_1=0}^{t_2=312} P(t)dt \Rightarrow W(\Delta t) = 2944.45\ J \ \rightarrow\ 181.61\ kJ/mole. \tag{7.3}$$

$$W(t) = \int_{t_1=291}^{t_2=312} P(t)dt \Rightarrow W(\Delta t) = 1008\ J \ \rightarrow\ 62.17\ kJ/mole. \tag{7.4}$$

Figure 7.2 depicts the variation of B_4C rhombohedral unit cell volume and current through the sample as a function of time under 3.8 V/mm. The unit cell volume variation is in agreement with current draw and follows all three stages that were observed as a function of time (see Fig. 7.1). From 0.1 A to 1 A, a 0.25% unit cell volume expansion is observed. The volumetric expansion corresponding to the rapid current draw from 1A to 10A is 0.66 % in 12 seconds.

Figure 7.3 depicts the time dependence of the B_4C unit cell volume change under 3.6 V/mm at constant temperature of 870^oC. The unit cell volume increases up to 870^oC with E=0 V/mm is due to thermal expansion which is not shown in the graph; here time scale was set to 0 from 870^oC (at the time at which e-field is applied) for illustration

purpose. B_4C unit cell volume is nearly invariant at 870°C under 0.0 V/mm electric field. However, unit cell started to expand with the application of 3.6 V/mm, which is accompanied by a 0.1 A current draw through sample. The expansion reached 0.36% during onset period (0.1-1A) in 288 seconds. In the transient stage, the B_4C unit cell undergoes a large expansion of 0.33% from 1A at 875°C to 10 A at 896.7°C in 21 seconds. The total unit cell expansion with the application of electric field is 0.7% as the current draw increases from 0.1 A to 10A. In both experiments, the unit cell shrinks with decreasing temperature as the sample is cooled to room temperature upon the completion of sintering (not shown here).

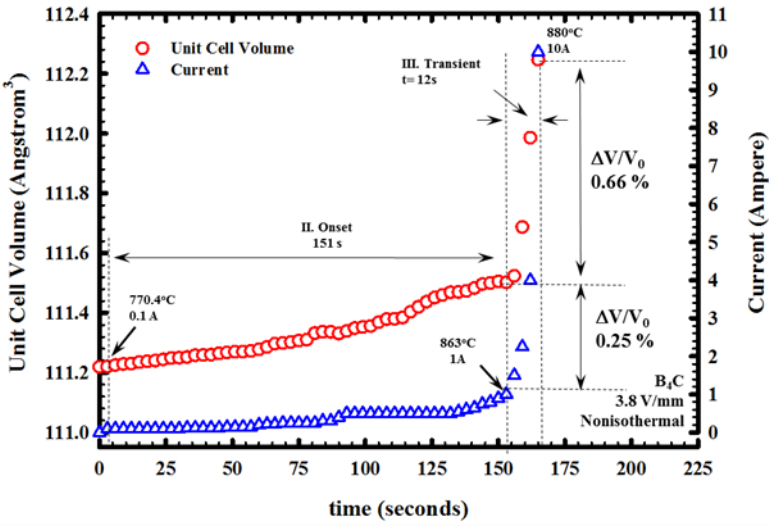

Figure 7. 2. The variation of the unit cell volume of B_4C and the current as a function of time during nonisothermal flash sintering under 3.8 V/mm.

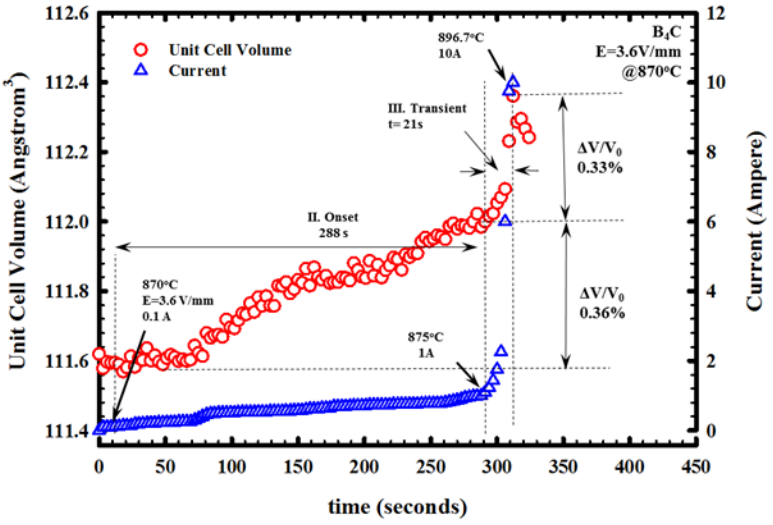

Figure 7. 3. The variation of the unit cell volume of B_4C and the current as a function of time during isothermal flash sintering under 3.6 V/mm.

The unit cell volume of rhombohedral B_4C between 0.1 and 10A as a function of time for non-isothermal and isothermal experiments is depicted together in Figure 7.4 for comparison purpose. Volumetric expansions during transient states are 0.66% in nonisothermal experiment, and 0.33% for isothermal experiment. Since there is not significant difference between power densities of two specimen, the difference between unit cell expansions can be caused by experimental conditions. The nonisothermal process also relies on the creation of a mass flux due to a temperature gradient, and ensure a transient state during $\vec{E}$ and ∇T induced mass transport. The isothermal process, on the other hand, does not permit for the temperature gradient effect, in addition, it supposes a steady state. The response of the unit cell differs markedly as a consequence.

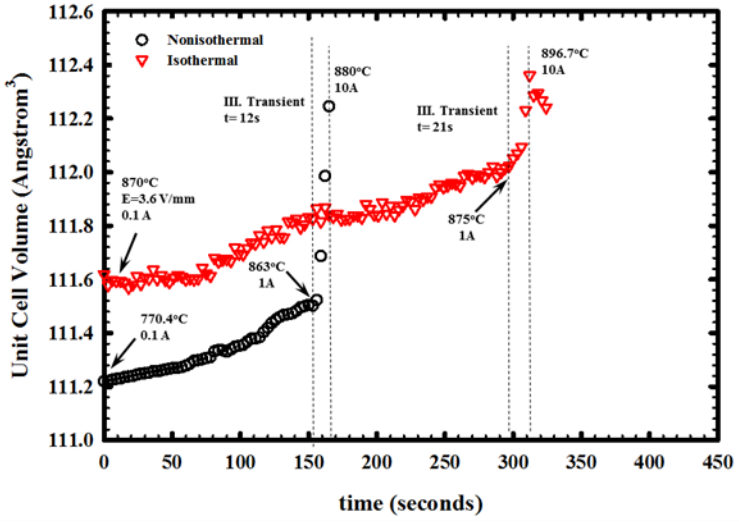

Figure 7. 4. The variation of unit cell volume of B_4C under non-isothermal and isothermal condition as a function of time.

Figure 7.5 shows the variation of rhombohedral angle of B_4C, peak broadening of the (021) reflection, and the current as a function of time for a) nonisothermal and b) isothermal condition. The rhombohedral angle of B_4C does not change with time under both 3.6 and 3.8 V/mm while unit cell volume increases as observed other experiments. The consistency of the rhombohedral angle is indicative of polycrystalline averaging an otherwise uniaxial crystal. No discontinuity at peak broadening is observed in the vicinity of the transient state. That is because structural changes associated with the migration of polarons under applied field are not detectable as a variations in full width at half maximum [104].

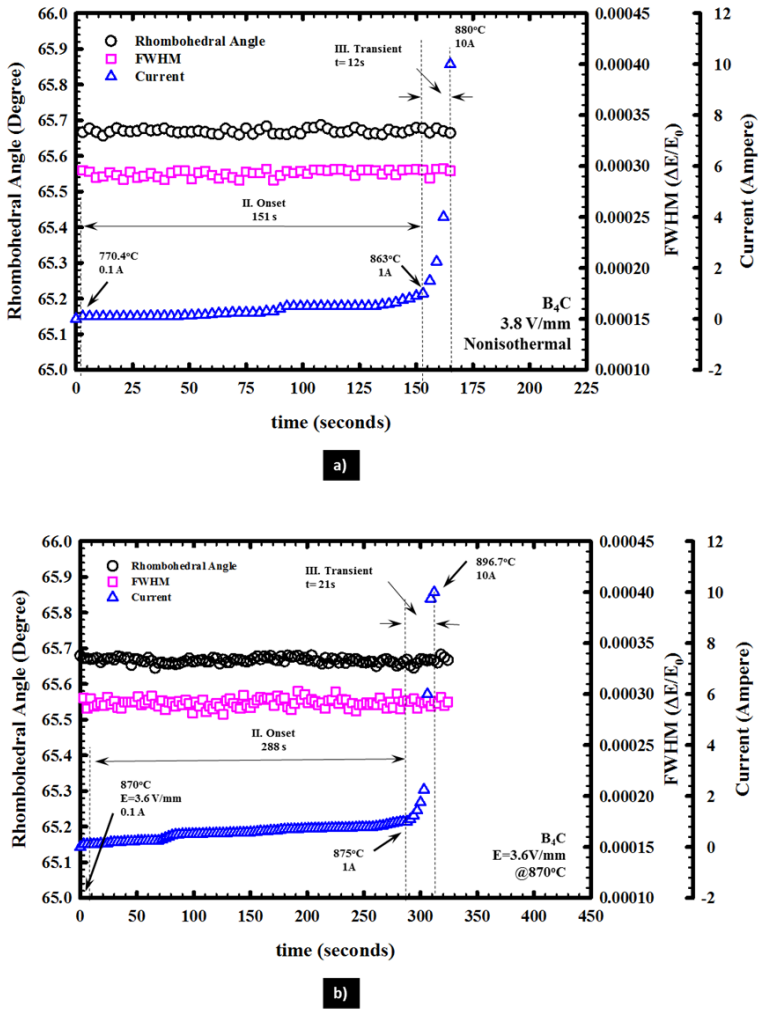

Figure 7. 5. The variation of the full width at half maximum (FWHM) of rhombohedral phase (021) reflection and rhombohedral angle of B_4C under a)nonisothermal 3.8 V/mm and b) isothermal 3.6 V/mm at the current range of 0.1-10Amperes.

Densities of the samples were measured with Archimedes method and were found to be 93% for the sample densified under nonisothermal condition with 3.8 V/mm and 92% for the one densified under isothermal condition with 3.6 V/mm.

7.1.2. Discussion and Conclusion

The significance of the experiments discussed in this chapter is that the system responded the applied electric field instantaneously with ≥ 0.1 A at 870^{o}C under isothermal condition. Sudden increase in current proofs that the system was ready to induce current drawn through sample following the choice of the electric field and the temperature based on non-isothermal experimental background. The remarkable point of the onset stage (0.1-1A) of the isothermal experiment is that temperature does not increase significantly while unit cell is expanding, determining that the unit cell expansion is directly coupling with current draw and not solely with joule heating.

The onset stage takes place ~13 times longer than transient state and temperature does not increase significantly in both stages. However, the total unit cell volume expansions in both stages are close to each other that again underlines the effect of the current driven unit cell expansion.

The power absorption by B_4C does not change in both experiments since applied electric fields are approximately same. However, the current driven unit cell expansion is higher in nonisothermal experiment due to the combined effect of heating and electric fields.

Moreover, we showed that the difference in experiment conditions does not alter the rhombohedral angle and line broadening behavior during sintering process.

7.2. Flash Sintering of B_4C under Different Electric Fields

The success of the densification of B_4C specimen under low electric fields at low temperatures leads us to repeat experiments under different electric fields for optimization of the burst mode densification process parameters. Therefore, we conducted several nonisothermal in-situ experiments at NSLS, BNL. The effect of the transient power increase in the crystal structure of boron carbide is explained in detail in the chapter 6 and we called such coupling phenomena as galvanomechanical effect in boron carbide system. In this section, the effect of electric field magnitude on the onset temperature and sintering density in the burst mode densification of B_4C will be reported.

7.2.1. Experimental

All samples were prepared under same conditions that were explained before. Thicknesses of the samples vary between ~2.5mm to 3mm. In the first experiment, the range of the 1.25 to 3.5 V/mm dc field was applied gradually while heating the sample with 30^{o}C/min, and data collection was carried out every 3 seconds. In the second run, B_4C specimen was heated with ~40^{o}C/min average heating rate under 3.8 V/mm applied dc field and data was collected with every 3 seconds time interval. Third experiment was performed under 4.5 V/mm dc field while heating the B_4C specimen with ~30^{o}C/min and data was collected with a Δt = 2 seconds. Fourth and fifth experiments were carried out with ~25^{o}C/min heating rate. Data from x-ray diffraction was collected with every 3 seconds and 2 seconds time interval for applied dc field of 5.3V/mm and 6.9 V/mm, respectively. Once the current hit its maximum of 10 A (limitation was set at the beginning), the system switches to current control by itself and undergoes the steady

state where power remains constant. The power source is turned off after short period of time once the system reaches steady state, and all specimen were cooled down to room temperature after removing dc field on sample. EDXRD setup was identical to the one reported earlier in section 4.

7.2.2. Results

Maximum power absorption by each B_4C specimen and temperatures corresponding to these power density values as a function of applied dc fields were depicted in Figure 7.6. The data in hand indicates that the electric field on sample is increased, the burst/sintering temperature decreased. The conductivity of the sample increases nonlinearly while heating that triggers the onset of rapid power rise according to ($W=V^2/R$; where W is power, V is voltage and R is resistance). Commensurately, one finds a direct correlation between applied electric field and the maximum power absorbed by the system, i.e. the higher the applied field, the higher the energy absorbed. (see Fig. 7.6).

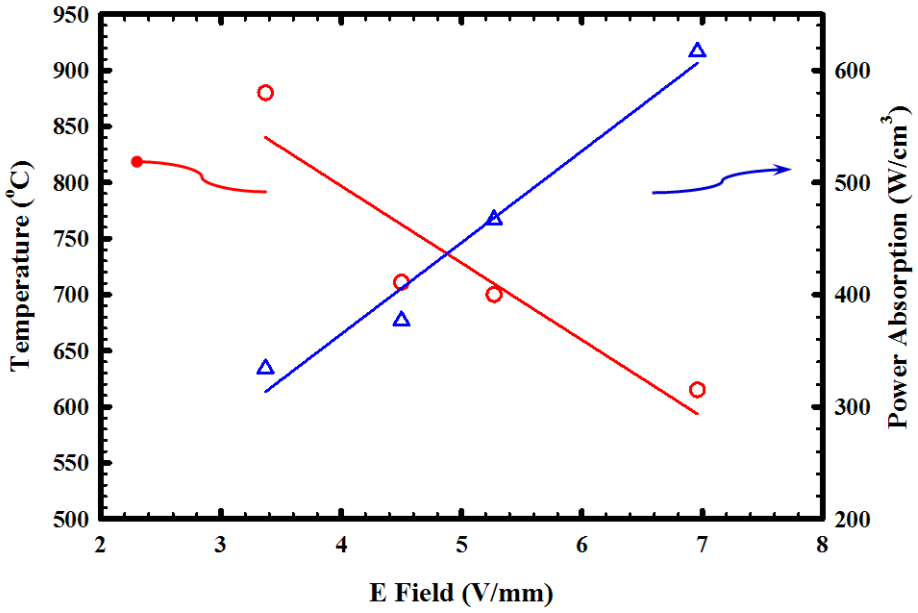

Figure 7. 6. The sintering temperature and power absorption by each B_4C specimen at current limitation of 10 A as a function of applied dc field.

Figure 7.7 depicts the temperature variation (7.7.a) and unit cell variation (7.7.b) of B_4C specimen for the applied dc field lower than 3 V/mm. The specimen was heated up to 1000°C under 1.25 V/mm and as seen from figure 7.7.a no current draw was observed at even 1000°C. Then system was reduced to 880°C and the dc field was increased gradually from 1.25 V/mm to 3 V/mm under isothermal conditions at 880°C (temperature was chosen according to previous experiments). Up to 3.5 V/mm electric field, no current was observed which shows that dc fields below 3.5 V/mm are not sufficient to induce current draw through B_4C despite the fact that the bulk electrical conductivity of the B_4C is appreciably high in this temperature range. We speculate that temperature values higher than 1000°C is required to observe current draw for electric field ≤ 3V/mm. Moreover, current observation at 880°C with the increase of electric fields higher than

3.5 V/mm provides information about repeatability of experiments. Figure 7.7(b) shows the unit cell expansion while heating the specimen under dc fields. Since there is no current flow during the experiment, unit cell expands solely due to thermal expansion up to 1000°C, and the observed shrinkage of cell volume is due to with cooling to 880°C. The unit cell volume of B_4C is stabilized at constant temperature in the 1.25 to 3.5 V/mm range without of any current draw (only shows 1.25-2.5V/mm range).

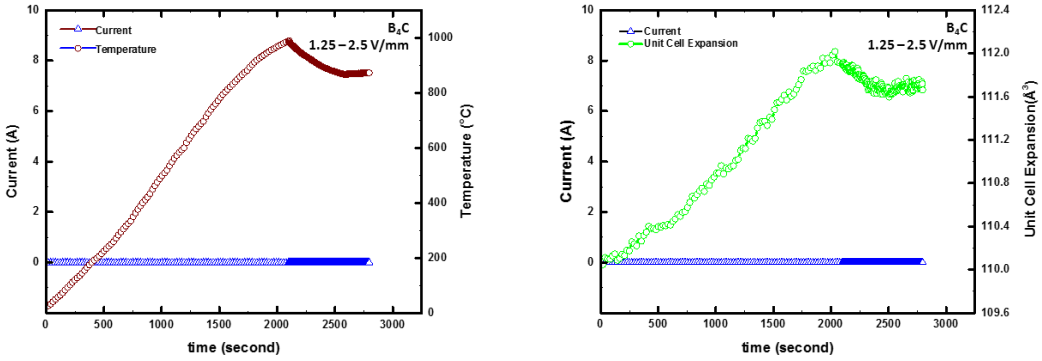

a) b)

Figure 7. 7. The temperature (a) and B_4C unit cell volume variation (b) as a function of time and current for the B_4C specimen under the dc field range of 1.25 - 2.5V/mm.

Figure 7.8 depicts the variation of the unit cell volume for each B_4C specimen under the electric fields of 3.8V/mm as a function of time. Under 3.8 V/mm, no current was observed and unit cell expansion is simply due to thermal expansion up to 1100 seconds and 770.4 °C, the slop of the unit cell volume expansion slightly changed due to < 1A current draw which took approximately 151 seconds. A sudden current rise started from 1A at 863.6°C, and reached to 10A at 880.4°C. The anomalous expansion is 0.66% during transient state for 3.8 V/mm applied dc field.

Figure 7.9 shows the unit cell volume of B_4C under 4.5 V/mm which was discussed in details at section 6. Here, up to 1000 seconds and 501^oC the current was ≤ 0.1A and started to slowly increase at 501^oC. The current reached to 0.74A at 688^oC in 296 seconds, and the slope of the unit cell expansion changed in a way that is reminiscent to the 3.8V/mm experiment. The rise in power reached its maximum at 711^oC. During the transient state (0.74A to 10A) which was 28 seconds in duration, the unit cell of B_4C expanded by 1.12%.

Figure 7.10 depicts the behavior of the unit cell volume of B_4C specimen under 5.3 V/mm. Up to 1700 seconds and 620^oC, current was < 0.1A. Once current draw started, it reached to 1 A at 683^oC, and to 10A at 700^oC. The current rise from 1-10A occurs in 18seconds, and corresponding to a unit cell expansion of 1.21%. The temperature increase in transient range is 17^oC for 5.3 V/mm.

The last experiment was carried out under 6.9V/mm (see Figure 7.11). Up to 1536 seconds, no current was observed. At 600^oC current draw started and reached to 10 A at 615^oC in 14 seconds. Such a rapid rise in current correlated with colossal 1.46 % unit cell expansion and 15^oC increase in temperature.

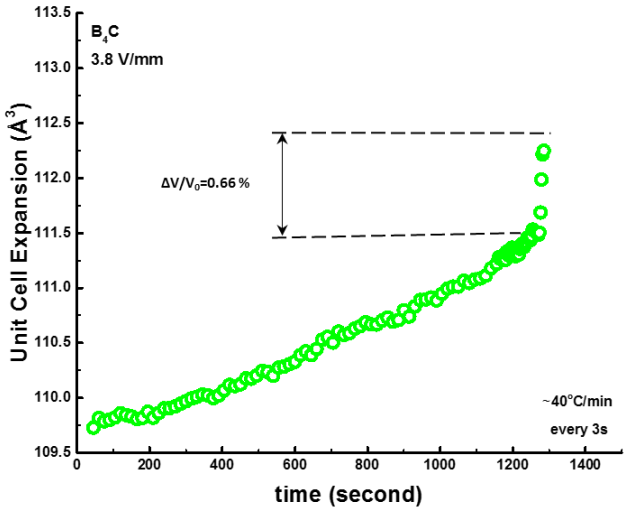

Figure 7. 8. The variation of the unit cell expansion of B_4C as a function of time under 3.8 V/mm.

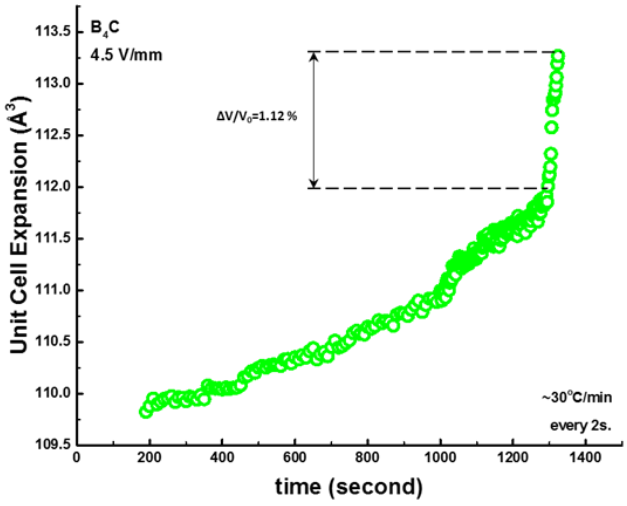

Figure 7. 9. The variation of the unit cell expansion of B_4C as a function of time under 4.5 V/mm.

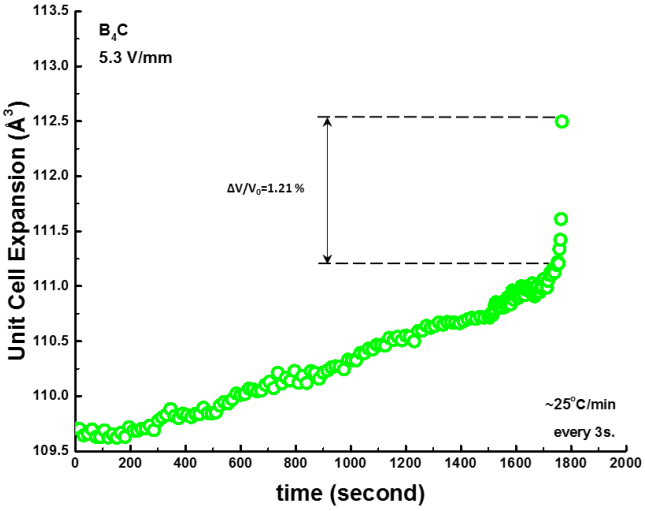

Figure 7. 10. The variation of the unit cell expansion of B_4C as a function of time under 5.3 V/mm.

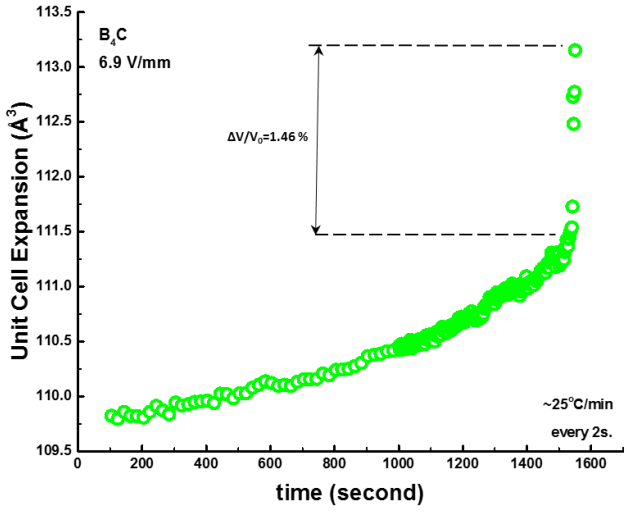

Figure 7. 11. The variation of the unit cell expansion of B_4C as a function of time under 5.3 V/mm.

The results indicate that one observes the abrupt rise in power absorption due to a precipitous current rise for all electric field magnitudes tested. An increase in the applied field's magnitude results in a shorter transient state but larger unit cell expansion.

The relation between the applied dc field and the current driven unit cell expansion is summarized in figure 7.12. The current driven colossal expansion of the B_4C unit cell volume obeys a power law type variation and closely tracks the power absorption by B_4C (see Fig. 7.6).

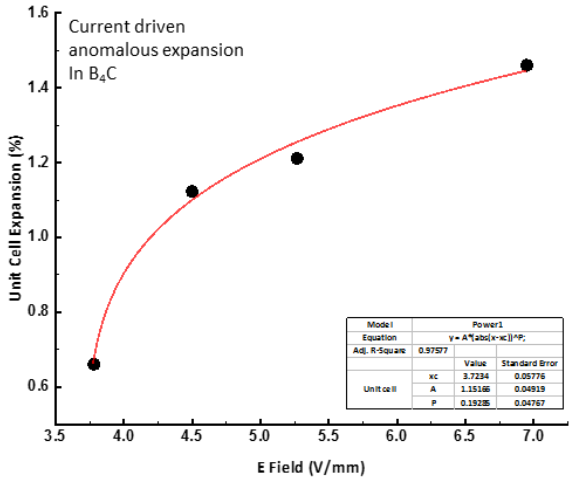

Figure 7. 12. Anomalous current driven unit cell volume expansion during transient state under different electric field.

In the previous chapters we have shown and elaborated on the fact that the angle of the rhombohedral unit cell of B_4C is invariant as a function of time in burst mode densification. We have further verified the invariance of the rhombohedral angle by running experiments as a function of applied electric field. No changes were observed (see Fig. 7.13).

The <012> peak width change with time as a function of electric field is depicted in Fig. 7.14 (limited time range at which current draw is observed was shown in figure). The peak width is also found to be invariant in all experiments as expected according to the results from Chapter 6. What we have shown here that the variation of the applied dc field does not affect the behavior of FWHM of the depicted peak, and confirm that the current-driven unit cell expansion is solely due to the burst of small polarons through the B_4C lattice, and not by the migration of point defects.

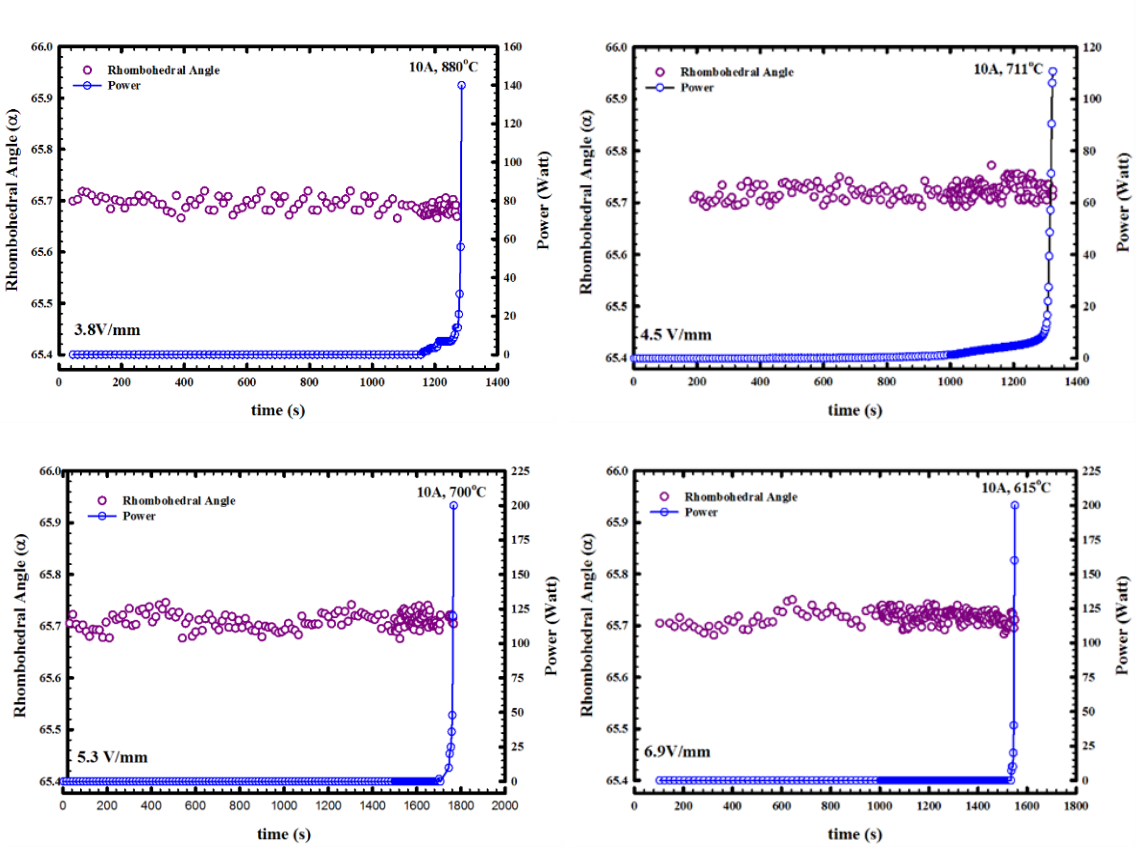

Figure 7. 13. The rhombohedral angle of the boron carbide unit cell as a function of time and corresponding power behavior for the applied dc field of 3.8 V/mm, 4.5 V/mm, 5.3 V/mm, and 6.9 V/mm.

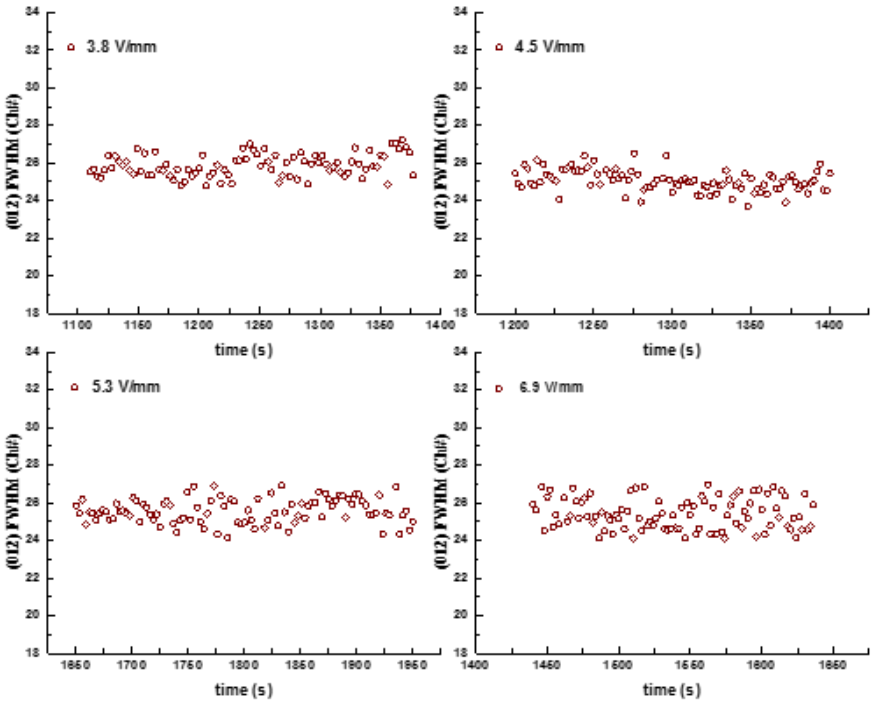

Figure 7. 14. The FWHM of (012) reflection as a function of time under electric and thermal field (data shown from limited ranges for illustration purposes).

As shown in the foregoing discussion, the application of the different electric fields vary the behavior of power-time relation while also reducing the onset temperature of burst mode densification. Power data as a function of time during transient stage for each dc field studied was plotted (see Fig. 7.13 for each specimen's power-time plot) and integrated to obtain the energy absorbed by each specimen. Such calculation revealed that specimen under 4.5 V/mm dc field absorbed more energy during transient stage which explains why the ΔT during burst mode densification is higher as compared to other applied fields. Table 7.1 summarizes transient stage response characteristics as a function of applied electric field.

Table 7. 1.The results of the integration of transient stage from power-time data for each experiment and corresponding experimental temperature rise.

E Field (V/mm)	T (°C) at 10A	Transient Stage (W.s)	Measured ΔT (°C)
3.8	880.4	556.5	12.2
4.5	711	1172.4	23
5.3	700	807	17
6.9	615	700	15

The potential joule heating during the transient state is analyzed in terms of temperature equivalent of thermal expansion of B_4C based on lattice parameter data obtained from the body center of the specimens. Table 7.2 shows the computed temperature values from thermal expansion coefficient of B_4C. The computed temperatures are represented the temperature rise needed to induce the observed unit cell volume change during transient power passing through specimens. The measurement of the variation of current driven unit cell volume with ultrahigh energy synchrotron probe as a function of temperature enable us to use the following relation for each experiment;

$$\Delta T = \frac{1}{\alpha_V^{B_4C}} \frac{\Delta V}{V_0} \tag{7.5}$$

where $\alpha_V^{B_4C}$ is the volumetric thermal expansion coefficient of the B_4C, and $\frac{\Delta V}{V_0}$ is the volumetric expansion of the unit cell, and ΔT is the fictitious temperature change corresponding to such unit cell volume variation. As seen from Table 7.2 ΔT is too low to induce mass transport based on Joule heating consideration alone. Most importantly, Δt of Stage III for each experiment is very short to complete densification which suggests that the cause of the burst mode densification should be sought elsewhere.

Table 7. 2**.** The summary of the results for galvanomecanical effect under different dc fields.

DC Field (V/mm)	Unit Cell Expansion (%)	Relative Density (%)	Calculated ΔT (^{o}C) from TEC	Calculated T increase rate (^{o}C/min)	Experimental ΔT (^{o}C)
3.8	0.66	93	392.9	1964.3	~12.2
4.5	1.12	95	666.7	1428.6	~23
5.3	1.211	94	696.4	3482.1	~17
6.9	1.46	94	869.0	3724.5	~15

Figure 7.15 shows the microstructures of flash sintered B_4C specimens under different electric fields. Since the density of specimens vary between 93-95%, microstructures of B_4C specimens show similarity. No grain growth is observed during all sintering processes because of eliminating steady state stage that causes joule heating and consequently grain growth.

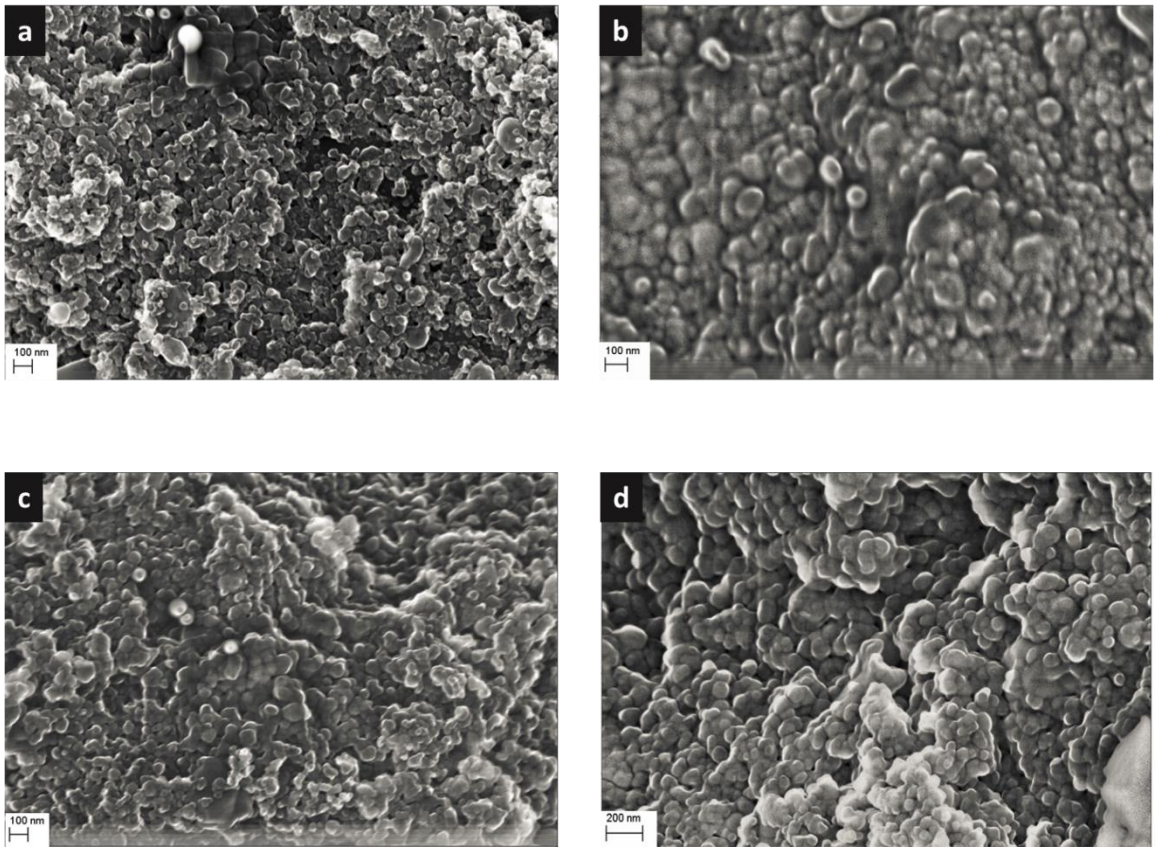

Figure 7. 15. Microstructure of pristine flash sintered B_4C specimen under a)3.8V/mm, b)4.5 V/mm, c)5.3 V/mm, and d)6.9 V/mm.

7.2.3. Discussion and Conclusion

We have provided more insight about newly discovered galvanomechanical phenomena during flash sintering of B_4C in this section. The understanding of the connection between the process variables and galvanomechanical effect enlightens the future of the flash sintering of covalent bonded ceramics. The work reported in this chapter reveals the following results; 1) the unit cell volume expands monotonically due to thermal expansion solely for each run before any current draw, 2) at different temperatures for each electric field, one singularity is observed in the variation of the unit

cell expansion as a function of time, and increase of dc field reduces sintering temperature, 3) the current driven colossal unit cell expansion undergoes typically in 12-28 seconds for 3.8-6.9 V/mm field range, and the magnitude of such expansion increases with the application of higher electric fields, 4) transient expansion is compromising with rapid rise of the power for each system and we called this phenomena as galvanomechanical effect in B_4C system. SEM images of B_4C specimen under different e-filed proof that grain growth is not observed in flash sintering of B_4C. The applied dc field contributes process as a driving force for nucleation, therefore; varying dc field differs the onset temperature and rate of the nucleation.

8. Conclusion and Future Work

The feasibility of flash sintering boron carbide has been investigated in this study. All experiments reported here were performed with a ultrahigh energy polychromatic synchrotron radiation with high temporal resolution to study variation at the unit cell parameters of B_4C accompanying the combined effect of temperature and electric field.

In the first part of this study, thermal expansion analysis of B_4C was investigated. Identical specimens were heated under different constant electric fields, and the effect of the electric field on thermal expansion coefficients of B_4C was reported. It was shown that increase in electric field strength causes increase in non-linearity of thermal expansion behavior of B_4C.

Secondly, in-situ flash sintering of B_4C have been carried out under different constant electric fields. We have shown that the densification of B_4C can be enhanced with flash sintering by 1-2 orders of magnitude at $T<0.3T_m$ with application of low electric

fields compared to other field assisted sintering techniques such as SPS. In-situ EDXRD experiments have revealed a solid state coupling mechanism between electric current and unit cell volume of B_4C, which we called the galvanomechanical effect (GME) [proposed by Dr. Akdogan]. The GME increases atomic transport rates in a highly covalent small polaron conductor because of anomalous current driven volumetric lattice expansion that is otherwise not possible with thermally activated atomic mobility. The microstructure of sintered specimen suggests that no grain growth is observed and this can be explained by transient nature of flash sintering. Joule heating during flash sintering is still arguable due to a large amount of transient power pass through material. However, the results of current driven unit cell expansion suggests that the colossal unit cell expansion of B_4C during transient state cannot be solely explained by joule heating.

The last part of the study was devoted to the effect of sintering condition. Non-isothermal and isothermal conditions alter the onset and transient time and unit cell expansion percentage during transient state. However, there is not strong effect on densification. Moreover, the effect of the electric field at flash sintering of B_4C was investigated. The increase of applied electric field reduced the sintering temperature. Also, increase of electrical field increases the unit cell expansion of rhombohedral B_4C.

Future work suggested after all results discussed herein as follows;

1. The continuous research is required to enhance densification of B_4C to higher densities and to analyze the mechanical properties of flash sintered B_4C comparing to other sintering techniques such as hot pressing and SPS. Higher power densities can be utilized to observe the effect on densification while keeping current limitation lower to

avoid any melting at the grain boundaries. Also, the flash sintering should be conducted for other covalent bonded materials to shed light into densification mechanisms in such ceramics.

2. Temperature measurement of the specimen during in-situ experiments were challenging, and temperature increase inside the specimen during transient state is still arguable. As a future work, new furnace design can be proposed to suggest best solution to measure temperature directly from specimen.

3. Pure B_4C nanoparticulate powder must be flash sintered to observe the effect of the free carbon on the densification in flash sintering and mechanical properties of B_4C.

Appendix 1

We have assumed that the system is adiabatic in Stage III, and that the electric to thermal energy conversion efficiency is 100%. This sweeping assumption implies that the power dissipated in Joule heating is entirely used for the needed thermal activation of the governing mass transport mechanism without heat loss to the surroundings. We now consider the power density $\Psi(t)$ absorbed by the system when an electric field ($\nabla\phi$=4.5 V/mm) is imposed on it which is given by $\Psi(t)=J(t)\,\nabla\phi(t)^3$, where J(t) is the current density due to $\nabla\phi$. The current-induced enthalpy increment $\Delta H(J)$ (normalized to one mole) can then be obtained from (in conjunction with **Fig. 6.1**)

$$\mathbf{\Delta H(J)} = \left(\frac{(\nabla\phi h)\pi r^2}{\left(m/\lambda\right)} \right) \int_0^t J(t)dt\,, \qquad \text{(A.1.1)}$$

where h is the sample thickness, r is the specimen radius, m is the specimen weight and λ is the molecular weight of the material of interest and t=28 seconds. The thermal enthalpy $\Delta H(T)$ increment associated with convectively heating the specimen to 711 ^{o}C is simply obtained using the isobaric heat capacity (χ_p) data via

$$\Delta H(T=984K) = \Delta H^{o}_{298K} + \int_{298K}^{984K} \chi_p dT \qquad \text{(A.1.2)}$$

The total adiabatic enthalpy increment due to (T, J) is then ΔH(T, J)= ΔH(J) + ΔH(T) which will lead to internal heating to a temperature that can be obtained by solving the following integral equation for the upper bound:

$$\left[\Delta H(J) + \Delta H(T = 984K)\right] = \Delta H^{o}_{298K} + \int_{298K}^{T^*} \chi_p dT \quad . \tag{A.1.3}$$

The temperature (T*) obtained upon solving Eq. (3) is the so-called adiabatic temperature rise due to current density J via Joule heating. This temperature is the theoretical limit that is unattainable because of the high thermal conductivity of B_4C [129-131].

Nonlinear regression to the segment of the unit cell volume (UCV) versus time data in Stage III revealed a third order time dependence of UCV on time, making the diffusivity a quadratic function of time [taken from the manuscript of the first article related to flash sintering of B_4C. Submission in progress by Dr. Akdogan & H. Bicer].

References

1. Beauvy, M. (1983). Stoichiometric limits of carbon-rich boron carbide phases. *Journal of the Less Common Metals*, *90*(2), 169-175.
2. Domnich, V., Reynaud, S., Haber, R. A., & Chhowalla, M. (2011). Boron carbide: structure, properties, and stability under stress. *Journal of the American Ceramic Society*, *94*(11), 3605-3628.
3. Andrievski, R. A. (2012). Micro-and nanosized boron carbide: synthesis, structure and properties. *Russian Chemical Reviews*, *81*(6), 549-559.
4. Vast, N., Sjakste, J., & Betranhandy, E. (2009, June). Boron carbides from first principles. In *Journal of Physics: Conference Series* (Vol. 176, No. 1, p. 012002). IOP Publishing.
5. Suri, A. K., Subramanian, C., Sonber, J. K., & Murthy, T. C. (2010). Synthesis and consolidation of boron carbide: a review. *International Materials Reviews*,*55*(1), 4-40.
6. Balakrishnarajan, M. M., Pancharatna, P. D., & Hoffmann, R. (2007). Structure and bonding in boron carbide: The invincibility of imperfections. *New Journal of Chemistry*, *31*(4), 473-485.
7. Wood, C., & Emin, D. (1984). Conduction mechanism in boron carbide. *Physical Review B*, *29*(8), 4582.
8. Cullity, B. D. (1978). Elements of X-ray Diffraction, 2nd. *Adisson-Wesley Publishing. USA*.
9. Aselage, T. L., & Tissot, R. G. (1992). Lattice constants of boron carbides. *Journal of the American Ceramic Society*, *75*(8), 2207-2212.
10. Thevenot, F. (1990). Boron carbide—a comprehensive review. *Journal of the European Ceramic Society*, *6*(4), 205-225.
11. Lipp, A. (1970). *Boron Carbide: Production, Properties, and Applications*. Battelle Northwest Laboratories.
12. Li, Y. Q., & Qiu, T. (2007). Oxidation behaviour of boron carbide powder.*Materials Science and Engineering: A*, *444*(1), 184-191.
13. Gogotsi, Y. G., Yaroshenko, V. P., & Porz, F. (1992). Oxidation resistance of boron carbide-based ceramics. *Journal of materials science letters*, *11*(5), 308-310.
14. Pilladi, T. R., Panneerselvam, G., Anthonysamy, S., & Ganesan, V. (2012). Thermal expansion of nanocrystalline boron carbide. *Ceramics International*, *38*(5), 3723-3728.
15. Prochazka, S., Dole, S. L., & Hejna, C. I. (1985). Abnormal grain growth and microcracking in boron carbide. *Journal of the American Ceramic Society*, *68*(9), C-235.
16. Matsui, T., Arita, Y., Naito, K., & Imai, H. (1991). High temperature heat capacities and electrical conductivities of boron carbides. *Journal of nuclear materials*, *186*(1), 7-12.
17. Wood, C., Zoltan, A., Emin, D., & Gray, P. E. (1985). Thermal conductivity behavior of boron carbides. In *Thermal Conductivity 18* (pp. 139-148). Springer US.

18. Moss, M. (1987, January). Thermal conductivity of boron carbides. In *MRS Proceedings* (Vol. 97, p. 77). Cambridge University Press.
19. Bouchacourt, M., & Thevenot, F. (1985). The correlation between the thermoelectric properties and stoichiometry in the boron carbide phase B4C-B10. 5C. *Journal of Materials science*, *20*(4), 1237-1247.
20. Ruh, R., Donaldson, K.Y., Hasselman, D.P.H. Thermal conductivity of boron carbide–boron nitride composites. J. Am. Ceram. Soc. 75, 2887-2890 (1992).
21. Werheit, H. (2007). Are there bipolarons in icosahedral boron-rich solids?.*Journal of Physics: Condensed Matter*, *19*(18), 186207.
22. Werheit, H. (2006). On excitons and other gap states in boron carbide. *Journal of Physics: Condensed Matter*, *18*(47), 10655.
23. Yamazaki, M. (1957). Electronic band structure of boron carbide. *The Journal of Chemical Physics*, *27*(3), 746-751.
24. Samara, G. A., Emin, D., & Wood, C. (1985). Pressure and temperature dependences of the electronic conductivity of boron carbides. *Physical Review B*, *32*(4), 2315.
25. Aselage, T. L., Emin, D., & McCready, S. S. (2001). Conductivities and Seebeck coefficients of boron carbides: Softening bipolaron hopping. *Physical Review B*, *64*(5), 054302.
26. Aselage, T. L., Emin, D., McCready, S. S., & Duncan, R. V. (1998). Large enhancement of boron carbides' seebeck coefficients through vibrational softening. *Physical review letters*, *81*(11), 2316.
27. Murthy, S. R. (1985). Elastic properties of boron carbide. *Journal of materials science letters*, *4*(5), 603-605.
28. Skorokhod, V., Vlajic, M. D., & Krstic, V. D. (1996). Mechanical properties of pressureless sintered boron carbide containing TiB 2 phase. *Journal of materials science letters*, *15*(15), 1337-1339.
29. B. Champagne and R. Angers, "Mechanical Properties of Hot Pressed B-B4C Materials," *Journal of the American Ceramic Society,* 62[3-4] 149=53 (1979).
30. K. A. Schwetz, L. S. Sigl, and L. Pfau, "Mechanical Properties of Injection Molded B4C-C Ceramics," *Journal of Solid State Chemistry,* 133 68-76 (1997).
31. F. C. L. de Melo, C. R. M. da Silva, A. H. A. Bressiani, and J. C. Bressiani, "Composition Effects on the Microstructure and Mechanical Properties of Sintered Boron Carbide," *Materials Science Forum,* 299-300 13-18 (1999).
32. Gogotsi, G. A., Gogotsi, Y. G., & Ostrovoj, D. Y. (1988). Mechanical behaviour of hot-pressed boron carbide in various atmospheres. *Journal of materials science letters*, *7*(8), 814-816.
33. Schwetz, K. A., & Grellner, W. (1981). The influence of carbon on the microstructure and mechanical properties of sintered boron carbide. Journal of the Less Common Metals, 82, 37-47.
34. Niihara, K., Nakahira, A., & Hirai, T. (1984). The effect of stoichiometry on mechanical properties of boron carbide. *Journal of the American Ceramic Society*, *67*(1), C-13.

35. Osipov, A. D., Ostapenko, I. T., Slezov, V. V., Tarasov, R. V., Podtykan, V. P., & Kartsev, N. F. (1982). Effect of porosity and grain size on the mechanical properties of hot-pressed boron carbide. *Soviet Powder Metallurgy and Metal Ceramics*, *21*(1), 55-58.
36. Palicka, R. J., & Negrych, J. A. (1989). *U.S. Patent No. 4,824,624*. Washington, DC: U.S. Patent and Trademark Office.
37. Thompson, R. (1966). *Borides: their chemistry and applications*. Royal Institute of Chemistry.
38. Matchen, B. (1996, September). Applications of ceramics in armor products. In*Key Engineering Materials* (Vol. 122, pp. 333-344).
39. Carter, C. B., & Norton, M. G. (2007). *Ceramic materials: science and engineering*. Springer Science & Business Media.
40. Vargas-Gonzalez, L., Speyer, R. F., & Campbell, J. (2010). Flexural strength, fracture toughness, and hardness of silicon carbide and boron carbide armor ceramics. *International Journal of Applied Ceramic Technology*, *7*(5), 643-651.
41. Goeuriot, P., Fillit, R., Thevenot, F., Driver, J. H., & Bruyas, H. (1982). The influence of alloying element additions on the boriding of steels. *Materials Science and Engineering*, *55*(1), 9-19.
42. Goeuriot, P., Thevenot, F., & Driver, J. H. (1981). Surface treatment of steels: Borudif, a new boriding process. *Thin Solid Films*, *78*(1), 67-76.
43. Jianxin, D. (2005). Erosion wear of boron carbide ceramic nozzles by abrasive air-jets. *Materials Science and Engineering: A*, *408*(1), 227-233.
44. Ridgway, R. R. (1934). Boron Carbide A New Crystalline Abrasive and Wear-Resisting Product. *Transactions of The Electrochemical Society*, *66*(1), 117-133.
45. Schwetz, K. A., Sigl, L. S., Greim, J., & Knoch, H. (1995). Wear of boron carbide ceramics by abrasive waterjets. *Wear*, *181*, 148-155.
46. Emin, D., & Aselage, T. L. (2005). A proposed boron-carbide-based solid-state neutron detector. *Journal of applied physics*, *97*(1), 013529.
47. Barney, W. K., Sehmel, G. A., & Seymour, W. E. (1958). The use of boron carbide for reactor control. *Nuclear Science and Engineering*, *4*(3), 439-448.
48. Rahaman, M. N. (1995). *Ceramic processing and sintering*. New York: Marcel Dekker.
49. Burke, J.E., Rosolowski, J.H. (1976). Sintering. In N.B. Hannay (Ed.), *Reactivity of Solids, Treatise on Solid State Chemistry* (pp. 621-659). New York: Plenum Press.
50. Burke, J. E. (1990). The development of pore-free ceramics, & Recrystallization and sintering in ceramics. In S. Somiya & Y. Moriyoshi (Eds.), *Sintering Key Papers* (pp. 3-38). Netherlands: Springer.
51. The Ceramic Society of Japan. (2012). Sintering. In Y. Imanaka et al. (Eds.), *Advanced Ceramic Technologies & Products* (pp. 19-22). Japan: Springer Science & Business Media.
52. Mackenzie, J. K., & Shuttleworth, R. (1949). A phenomenological theory of sintering. *Proceedings of the Physical Society. Section B*, *62*(12), 833.

53. Kingery, W. D., & Berg, M. (1955). Study of the initial stages of sintering solids by viscous flow, evaporation-condensation, and self-diffusion. *Journal of Applied Physics*, *26*(10), 1205-1212.
54. Coble, R. L. (1961). Sintering crystalline solids. I. Intermediate and final state diffusion models. *Journal of applied physics*, *32*(5), 787-792.
55. Geach, G. A. (1953). The theory of sintering. *Progress in Metal physics*, *4*, 174-204.
56. Greenough, A. P. (1950). Grain boundaries and sintering.
57. Kuczynski, G. C. (1956). The mechanism of densification during sintering of metallic particles. *Acta Metallurgica*, *4*(1), 58-61.
58. German, R. M. (2010). Coarsening in sintering: grain shape distribution, grain size distribution, and grain growth kinetics in solid-pore systems. *Critical reviews in solid state and materials sciences*, *35*(4), 263-305.
59. DeJonghe, C. L., Rahaman, M. N. (2003). Sintering of ceramics. In S. Somiya et al. (Eds.), *Handbook of Advanced Ceramics* (pp. 187-264). Elsevier Inc.
60. Bengisu, M. (Ed.). (2001). *Engineering ceramics*. Springer Science & Business Media.
61. Thevenot, F. (1988). Sintering of boron carbide and boron carbide-silicon carbide two-phase materials and their properties. *Journal of Nuclear Materials*, *152*(2), 154-162.
62. Angers, R., & Beauvy, M. (1984). Hot-pressing of boron carbide. *Ceramics international*, *10*(2), 49-55.
63. Roszeitis, S., Feng, B., Martin, H. P., & Michaelis, A. (2014). Reactive sintering process and thermoelectric properties of boron rich boron carbides.*Journal of the European Ceramic Society*, *34*(2), 327-336.
64. Kalandadze, G. I., Shalamberidze, S. O., & Peikrishvili, A. B. (2000). Sintering of boron and boron carbide. *Journal of Solid State Chemistry*, *154*(1), 194-198.
65. Larker, H. T. (1984). Dense ceramic parts hot pressed to shape by HIP. In*Emergent process methods for high-technology ceramics* (pp. 571-582). Springer US.
66. Sano, T., Chin, E. S. C., Paliwal, B., & Chen, M. W. (2009). Comparison of slip cast and hot pressed boron carbide. *Processing and properties of advanced ceramics and composites: ceramic transactions*, *203*, 107.
67. Munir, Z. A., Anselmi-Tamburini, U., & Ohyanagi, M. (2006). The effect of electric field and pressure on the synthesis and consolidation of materials: a review of the spark plasma sintering method. *Journal of Materials Science*, *41*(3), 763-777.
68. Garay, J. E. (2010). Current-activated, pressure-assisted densification of materials. *Annual review of materials research*, *40*, 445-468.
69. Lu, K. (2008). Sintering of nanoceramics. *International Materials Reviews*, *53*(1), 21-38.
70. Guillon, O., Gonzalez-Julian, J., Dargatz, B., Kessel, T., Schierning, G., Räthel, J., & Herrmann, M. (2014). Field-Assisted Sintering Technology/Spark Plasma Sintering: Mechanisms, Materials, and Technology Developments.*Advanced Engineering Materials*, *16*(7), 830-849.

71. Langer, J., Hoffmann, M. J., & Guillon, O. (2009). Direct comparison between hot pressing and electric field-assisted sintering of submicron alumina. *Acta Materialia*, *57*(18), 5454-5465.
72. Anselmi-Tamburini, U., Munir, Z. A., Kodera, Y., Imai, T., & Ohyanagi, M. (2005). Influence of synthesis temperature on the defect structure of boron carbide: experimental and modeling studies. *Journal of the American Ceramic Society*, *88*(6), 1382-1387.
73. Xu, C., Cai, Y., Flodström, K., Li, Z., Esmaeilzadeh, S., & Zhang, G. J. (2012). Spark plasma sintering of B 4 C ceramics: the effects of milling medium and TiB 2 addition. *International Journal of Refractory Metals and Hard Materials*,*30*(1), 139-144.
74. Hayun, S., Paris, V., Dariel, M. P., Frage, N., & Zaretzky, E. (2009). Static and dynamic mechanical properties of boron carbide processed by spark plasma sintering. *Journal of the European Ceramic Society*, *29*(16), 3395-3400.
75. Hayun, S., Kalabukhov, S., Ezersky, V., Dariel, M. P., & Frage, N. (2010). Microstructural characterization of spark plasma sintered boron carbide ceramics. *Ceramics international*, *36*(2), 451-457.
76. Lee, H., & Speyer, R. F. (2003). Pressureless sintering of boron carbide.*Journal of the American Ceramic Society*, *86*(9), 1468-1473.
77. Mashhadi, M., Taheri-Nassaj, E., & Sglavo, V. M. (2010). Pressureless sintering of boron carbide. *Ceramics International*, *36*(1), 151-159.
78. Lange, R. G., Munir, Z. A., & Holt, J. B. (1979). *Sintering kinetics of pure and doped boron carbide* (No. UCRL-82515; CONF-790682-3). California Univ., Livermore (USA). Lawrence Livermore Lab..
79. Dole, S. L., Prochazka, S., & Doremus, R. H. (1989). Microstructural coarsening during sintering of boron carbide. *Journal of the American Ceramic Society*, *72*(6), 958-966.
80. Bougoin, M., & Thevenot, F. (1987). Pressureless sintering of boron carbide with an addition of polycarbosilane. *Journal of materials science*, *22*(1), 109-114.
81. Kouzeli, M., San Marchi, C., & Mortensen, A. (2002). Effect of reaction on the tensile behavior of infiltrated boron carbide–aluminum composites. *Materials Science and Engineering: A*, *337*(1), 264-273.
82. Speyer, R. F., & Lee, H. (2004). Advances in pressureless densification of boron carbide. *Journal of materials science*, *39*(19), 6017-6021.
83. Lee, H. (2000). *Sintering of boron carbide* (Doctoral dissertation). Retrieved from ProQuest Dissertation & thesis A&I. (304620238).
84. Dole, S. L., & Prochazka, S. (1985, January). Densification and microstructure development in boron carbide. In *Proceedings of the 9th Annual Conference on Composites and Advanced Ceramic Materials: Ceramic Engineering and Science Proceedings, Volume 6, Issue 7/8* (pp. 1151-1160). John Wiley & Sons, Inc..
85. Yang, D., Raj, R., & Conrad, H. (2010). Enhanced Sintering Rate of Zirconia (3Y-TZP) Through the Effect of a Weak dc Electric Field on Grain Growth.*Journal of the American Ceramic Society*, *93*(10), 2935-2937.

86. Trombin, F., & Raj, R. (2014). Developing processing maps for implementing flash sintering into manufacture of whiteware ceramics. *American Ceramic Society Bulletin, 93*(6), 32-35.
87. Cologna, M., Rashkova, B., & Raj, R. (2010). Flash Sintering of Nanograin Zirconia in< 5 s at 850 C. *Journal of the American Ceramic Society*, *93*(11), 3556-3559.
88. Cologna, M., Prette, A. L., & Raj, R. (2011). Flash-Sintering of Cubic Yttria-Stabilized Zirconia at 750° C for Possible Use in SOFC Manufacturing. *Journal of the American Ceramic Society*, *94*(2), 316-319.
89. Hao, X., Liu, Y., Wang, Z., Qiao, J., & Sun, K. (2012). A novel sintering method to obtain fully dense gadolinia doped ceria by applying a direct current.*Journal of Power Sources*, *210*, 86-91.
90. Cologna, M., Francis, J. S., & Raj, R. (2011). Field assisted and flash sintering of alumina and its relationship to conductivity and MgO-doping. *Journal of the European Ceramic Society*, *31*(15), 2827-2837.
91. Prette, A. L., Cologna, M., Sglavo, V., & Raj, R. (2011). Flash-sintering of Co 2 MnO 4 spinel for solid oxide fuel cell applications. *Journal of Power Sources*,*196*(4), 2061-2065.
92. Karakuscu, A., Cologna, M., Yarotski, D., Won, J., Francis, J. S., Raj, R., & Uberuaga, B. P. (2012). Defect Structure of Flash-Sintered Strontium Titanate.*Journal of the American Ceramic Society*, *95*(8), 2531-2536.
93. M'Peko, J. C., Francis, J. S., & Raj, R. (2014). Field-assisted sintering of undoped BaTiO 3: Microstructure evolution and dielectric permittivity. *Journal of the European Ceramic Society*, *34*(15), 3655-3660.
94. Muccillo, R., & Muccillo, E. N. S. (2014). Electric field-assisted flash sintering of tin dioxide. *Journal of the European Ceramic Society*, *34*(4), 915-923.
95. Zapata-Solvas, E., Bonilla, S., Wilshaw, P. R., & Todd, R. I. (2013). Preliminary investigation of flash sintering of SiC. *Journal of the European Ceramic Society*, *33*(13), 2811-2816.
96. Naik, K. S., Sglavo, V. M., & Raj, R. (2014). Flash sintering as a nucleation phenomenon and a model thereof. Journal of the European Ceramic Society, 34(15), 4063-4067.
97. Lebrun, J. M., Morrissey, T. G., Francis, J. S., Seymour, K. C., Kriven, W. M., & Raj, R. (2015). Emergence and Extinction of a New Phase During On–Off Experiments Related to Flash Sintering of 3YSZ. *Journal of the American Ceramic Society*.
98. Francis, J. S., & Raj, R. (2013). Influence of the field and the current limit on flash sintering at isothermal furnace temperatures. *Journal of the American Ceramic Society*, *96*(9), 2754-2758.
99. Raj, R. (2012). Joule heating during flash-sintering. *Journal of the European Ceramic Society*, *32*(10), 2293-2301.
100. Francis, J. S. C. (2013). *A study on the phenomena of flash-sintering with tetragonal zirconia* (Doctoral dissertation, University of Colorado at Boulder).
101. Holland, T. B., Anselmi-Tamburini, U., & Mukherjee, A. K. (2013). Electric fields and the future of scalability in spark plasma sintering. *Scripta Materialia*,*69*(2), 117-121.

102. Orru, R., Licheri, R., Locci, A. M., Cincotti, A., & Cao, G. (2009). Consolidation/synthesis of materials by electric current activated/assisted sintering. *Materials Science and Engineering: R: Reports*, *63*(4), 127-287.
103. Savkliyildiz, I. (2015). In-situ energy dispersive x-ray diffraction study of pressure and electric field effects in the densification of ceramic oxide nanoparticles. (Doctoral dissertation, Rutgers University).
104. Akdoğan, E. K., Şavklıyıldız, İ., Biçer, H., Paxton, W., Toksoy, F., Zhong, Z., & Tsakalakos, T. (2013). Anomalous lattice expansion in yttria stabilized zirconia under simultaneous applied electric and thermal fields: A time-resolved in situ energy dispersive x-ray diffractometry study with an ultrahigh energy synchrotron probe. *Journal of Applied Physics*, *113*(23), 233503.
105. Clegg, W. (2000). Synchrotron chemical crystallography. *Journal of the Chemical Society, Dalton Transactions*, (19), 3223-3232.
106. Bassett, W. A., & Brown Jr, G. E. (1990). Synchrotron radiation-Applications in the earth sciences. *Annual Review of Earth and Planetary Sciences*, 18, 387-447.
107. Pecharsky, V. K., & Zavalij, P. Y. (2009). *Fundamentals of powder diffraction and structural characterization of materials* (Vol. 2). New York: Springer.
108. Buras, B., & Gerward, L. (1989). Application of X-ray energy-dispersive diffraction for characterization of materials under high pressure. Progress in Crystal Growth and Characterization, 18, 93-13
109. Buras, B., Olsen, J. S., & Gerward, L. (1976). X-ray energy-dispersive powder diffractometry using synchrotron radiation. Nuclear Instruments and Methods, 135(1), 193-195.
110. Kämpfe, B., Luczak, F., & Michel, B. (2006). Energy Dispersive X-Ray Diffraction. Particle & Particle Systems Characterization, 22(6), 391-396.
111. H. P. Klug and L. E. Alexander, X-Ray Diffraction Procedures: For Polycrystalline and Amorphous Materials (John Wiley & Sons, New York, 1974).
112. Guinier, X-ray Diffraction: In Crystals, Imperfect Crystals, and Amorphous Bodies (Dover Publications, Mineola, NY, 1994).
113. Croft, M., Zakharchenko, I. (2002). Strain field and scattered intensity profiling with energy dispersive x-ray scattering. *Journal of applied physics*, *92*(1), 578-586.
114. Croft, M., Jisrawi, N. (2008). Stress gradient induced strain localization in metals: High resolution strain cross sectioning via synchrotron x-ray diffraction. *Journal of Engineering Materials and Technology*, *130*(2), 021005.
115. Croft, M., Shukla, V. (2009). Mapping and load response of overload strain fields: Synchrotron X-ray measurements. *International Journal of Fatigue*, *31*(11), 1669-1677.
116. Tsakalakos, T., Croft, M. (2006, January). Measurement of residual stress distributions by energy dispersive X-ray diffraction synchrotron radiation. In *The Sixteenth International Offshore and Polar Engineering Conference*. International Society of Offshore and Polar Engineers.

117. Akdoğan, E. K., Şavklıyıldız, İ. (2012). Pressure effects on phase equilibria and solid solubility in MgO-Y2O3 nanocomposites. *Journal of Applied Physics*, *111*(5), 053506.
118. Akdoğan, E. K., Şavklıyıldız, İ. (2011). High-pressure phase transformations in MgO-Y2O3 nanocomposites. *Applied Physics Letters*, *99*(14), 141915.
119. Şavklıyıldız, İ., Akdoğan, E. K. (2013). Phase transformations in hypereutectic MgO-Y2O3 nanocomposites at 5.5 GPa. *Journal of Applied Physics*, *113*(20), 203520.
120. Toksoy, F. (2014). Densification of rapid carbothermal synthesized and commercial boron carbide by spark plasma sintering. (Doctoral dissertation, Rutgers University).
121. Holland, T. J. B., & Redfern, S. A. T. (1997). Unit cell refinement from powder diffraction data; the use of regression diagnostics. *Mineralogical Magazine*, *61* (1), 65-77.
122. Ho, C. Y., & Taylor, R. E. (Eds.). (1998). *Thermal expansion of solids* (Vol. 4). ASM international.
123. Tsagareishvili, G. V., Nakashidze, T. G. (1986). Thermal expansion of boron and boron carbide. *Journal of the Less Common Metals*, *117*(1), 159-161.
124. Messing, G.L., Stevenson, A. J., (2008). Towards pore-free ceramics. *Science* 322, 383.
125. Zapata-Solvas, E., Gómez-García, D., Domínguez-Rodríguez, A., & Todd, R. (2015). I. Ultra-fast and energy-efficient sintering of ceramics by electric current concentration. *Scientific reports* 5, 8513.
126. Reddy, K. M., et al. (2012). Enhanced mechanical properties of nanocrystalline boron carbide by nanoporosity and interface phases. *Nature. Commun.* 3**,** 1052.
127. Thompson, D.P., (2002). Materials science: Cooking up tougher ceramics. *Nature* 417, 237.
128. Chen, I.-W., Wang, X.-H, (2000). Sintering dense nanocrystalline ceramics without final-stage grain growth. *Nature* 404, 168-171.
129. Nowick, A.S., Berry, B.S., *Anelastic Relaxation in Crystalline Solids* (Academic Press, 1972).
130. Newnham, R.E., *Properties of Materials: Anisotropy, Symmetry, Structure.* (Oxford University Press, 2005).
131. Krivoglaz, M.A., *X-Ray and Neutron Diffraction in Nonideal Crystals.* (Springer, 1996).
132. Glicksman, M.E., *Diffusion in Solids: Field Theory, Solid-State Principles, and Applications* (John Wiley & Sons Inc., 2000).
133. Xie, X., et al. (2010). An asymemetrically surface-modified graphene film electrochemical actuator. *ACS Nano* 4, 6050-6054.
134. Gu, G., et al.(2003). V_2O_5 nanofiber sheet actuators. *Nature Mater.* 2, 316-319.
135. Baughham, R.H., et al. (1999). Carbon nanotube actuators. *Science* 284, 1340-1344.

136. E. K. Akdogan and Z. Zhong, private communication (2013).
137. Sairam, K., et al. (2014). Influence of spark plasma sintering parameters on densification and mechanical properties of boron carbide. *International Journal of Refractory Metals and Hard Materials*, *42*, 185-192.